Taylor & Francis
Taylor & Francis Group

RESEARCH PAPER

OPEN ACCESS   Check for updates

Converging roles of PSENEN/PEN2 and CLN3 in the autophagy-lysosome system

Marcel Klein[a,1], Abuzar Kaleem[a,1], Sandra Oetjen[a,1], Daniela Wünkhaus[b], Lars Binkle[c], Sandra Schilling[d], Milena Gjorgjieva[a], Ralf Scholz[a], Doris Gruber-Schoffnegger[b], Stephan Storch[e], Stefan Kins[d], Gerard Drewes[f], Sabine Hoffmeister-Ullerich[g], Dietmar Kuhl[a], and Guido Hermey [a]

[a]Institute for Molecular and Cellular Cognition, Center for Molecular Neurobiology Hamburg, University Medical Center Hamburg-Eppendorf, Hamburg, Germany; [b]Evotec SE, Manfred Eigen Campus, Hamburg, Germany; [c]Institute of Neuroimmunology and Multiple Sclerosis, Center for Molecular Neurobiology Hamburg, University Medical Center Hamburg-Eppendorf, Hamburg, Germany; [d]Division of Human Biology and Human Genetics, University of Kaiserslautern, Kaiserslautern, Germany; [e]Department of Pediatrics, University Medical Center Hamburg-Eppendorf, Hamburg, Germany; [f]Cellzome, Functional Genomics Research and Development, Heidelberg, Germany; [g]Bioanalytics, Center for Molecular Neurobiology Hamburg, University Medical Center Hamburg-Eppendorf, Hamburg, Germany

ABSTRACT

PSENEN/PEN2 is the smallest subunit of the γ-secretase complex, an intramembrane protease that cleaves proteins within their transmembrane domains. Mutations in components of the γ-secretase underlie familial Alzheimer disease. In addition to its proteolytic activity, supplementary, γ-secretase independent, functions in the macroautophagy/autophagy-lysosome system have been proposed. Here, we screened for PSENEN-interacting proteins and identified CLN3. Mutations in *CLN3* are causative for juvenile neuronal ceroid lipofuscinosis, a rare lysosomal storage disorder considered the most common neurodegenerative disease in children. As mutations in the *PSENEN* and *CLN3* genes cause different neurodegenerative diseases, understanding shared cellular functions of both proteins might be pertinent for understanding general cellular mechanisms underlying neurodegeneration. We hypothesized that CLN3 modulates γ-secretase activity and that PSENEN and CLN3 play associated roles in the autophagy-lysosome system. We applied CRISPR gene-editing and obtained independent isogenic HeLa knockout cell lines for *PSENEN* and *CLN3*. Following previous studies, we demonstrate that PSENEN is essential for forming a functional γ-secretase complex and is indispensable for γ-secretase activity. In contrast, CLN3 does not modulate γ-secretase activity to a significant degree. We observed in *PSENEN*- and *CLN3*-knockout cells corresponding alterations in the autophagy-lysosome system. These include reduced activity of lysosomal enzymes and lysosome number, an increased number of autophagosomes, increased lysosome-autophagosome fusion, and elevated levels of TFEB (transcription factor EB). Our study strongly suggests converging roles of PSENEN and CLN3 in the autophagy-lysosome system in a γ-secretase activity-independent manner, supporting the idea of common cytopathological processes underlying different neurodegenerative diseases.

Abbreviations: Aβ, amyloid-beta; AD, Alzheimer disease; APP, amyloid precursor protein; ATP5MC, ATP synthase membrane subunit c; DQ-BSA, dye-quenched bovine serum albumin; ER, endoplasmic reticulum; GFP, green fluorescent protein; ICC, immunocytochemistry; ICD, intracellular domain; JNCL, juvenile neuronal ceroid lipofuscinosis; KO, knockout; LC3, microtubule associated protein 1 light chain 3; NCL, neuronal ceroid lipofuscinoses; PSEN, presenilin; PSENEN/PEN2: presenilin enhancer, gamma-secretase subunit; TAP, tandem affinity purification; TEV, tobacco etch virus; TF, transferrin; WB, Western blot; WT, wild type.

Introduction

PSENEN/PEN2 (presenilin enhancer, gamma-secretase subunit) is the smallest subunit of the γ-secretase complex, an intramembrane protease that cleaves type-I transmembrane proteins within their transmembrane domains. γ-secretase is composed of four subunits, PSENEN, NCSTN (nicastrin), a variant of APH1 (aph-1 homolog, gamma-secretase subunit) and PSEN1 (presenilin 1) or PSEN2 (presenilin 2), which harbor the catalytic site [1–3]. All subunits of the γ-secretase complex are transmembrane proteins translated at the endoplasmic reticulum (ER), where the complex assembles [1]. PSENEN is the last subunit that joins the γ-secretase complex.

It binds PSEN and facilitates its endoproteolysis, thereby conferring γ-secretase activity [2,3].

A large number of type-I transmembrane proteins serve as γ-secretase substrates, such as NOTCH1 and APP (amyloid precursor protein). Following sequential cleavage of APP by α- or BACE/β-secretase and γ-secretase, the proteolytic products – including amyloid-beta (Aβ) and the APP intracellular domain – are released extracellularly and intracellularly, respectively [4–6]. Mutations in components of the γ-secretase complex cause familial Alzheimer disease (AD) [7]. Most of these mutations result in an increase in the production of Aβ, which can accumulate in the brain and is thought as a primary cause of AD. Apart from the mutations

causing AD, other mutations in *PSENEN, PSEN1* and *NCSTN* have been reported to cause *acne inversa*, a chronic inflammatory disease of hair follicles [8]. It has been suggested that the molecular pathogenesis implicates the γ-secretase-NOTCH pathway [8]. Upon cleavage by γ-secretase the NOTCH1 intracellular domain translocates to the nucleus, acts as a transcriptional activator and regulates cell fate [9]. Aside from APP and NOTCH1, γ-secretase cleaves a large number of other physiologically relevant substrates such as CDH1 (cadherin 1), the receptor tyrosine kinase ERBB4 and NGFR/p75NTR (nerve growth factor receptor), and signaling of these multiple proteolytic substrates are likely to be modulated by γ-secretase [10].

In addition to its proteolytic function, supplementary, γ-secretase independent, functions of PSENs in the autophagy-lysosome system have been proposed [11–14]. Cells co-express differing γ-secretase complexes, including either PSEN1 or PSEN2. PSEN1-containing complexes are broadly distributed in the cell, and several partially controversial studies suggest that PSEN1 regulates lysosomal function [11,15–19]. In contrast, PSEN2 harbors a lysosomal targeting signal and is targeted to late endosomes and lysosomes, but its lysosomal function is poorly described [20,21]. Moreover, lysosomal dysfunction has been implicated as a driver of increased amyloidogenic processing or incomplete Aβ degradation and may be one mechanism underlying sporadic AD [12,18]. Yet, PSENEN has not been studied in the context of macroautophagy (hereafter referred to as autophagy) and lysosomal function.

Here, we performed a tandem-affinity-purification (TAP)-tag screen to identify additional PSENEN interacting proteins. We found CLN3, a protein with six predicted transmembrane domains and the N and C termini facing the cytoplasm [22,23]. Mutations in CLN3 are causative for juvenile neuronal ceroid lipofuscinosis (JNCL) or CLN3 disease [24]. The disease belongs to the neuronal ceroid lipofuscinoses (NCLs), a group of rare lysosomal storage disorders considered the most common neurodegenerative disease in children characterized by gradual neurodegeneration. The age of disease onset differs between defined subtypes caused by mutations in different genes (*CLN1* to *CLN8; CLN10* to *CLN14*) [25,26]. The pathological hallmark is the intracellular accumulation of lysosomal autofluorescent storage material, so-called lipofuscin. These deposits are found in neurons and are as well abundant in non-neuronal cells outside the nervous system. Depending on the subtype, the storage material is either predominantly composed of ATP5MC (ATP synthase membrane subunit c) or the sphingolipid activator proteins A and D [23]. Further, the storage material can comprise to a different degree additional components such as the lysosomal proteins PPT1 (palmitoyl-protein thioesterase 1), TPP1 (tripeptidyl peptidase 1), and CTSD (cathepsin D) [27], and strikingly, accumulation of Aβ has been reported in some cases [28–30]. More recently, the examination of unexplained AD cases identified a genomic region directly upstream of the *CLN3* gene using genetic linkage analysis [31] and a missense variant in *CLN5* by whole-exome sequencing [32].

The classical juvenile form of NCL, JNCL or CLN3 disease, manifests mostly at the age of about six years in affected children with normal early development [25,26]. Clinical symptoms include progressive blindness, cognitive decline frequently accompanied by epileptic seizures, loss of motor function and a significantly reduced lifespan. JNCL is inherited in an autosomal recessive manner and about 60 different mutations in *CLN3* have been identified in affected individuals to date. The most frequent mutation, found in about 80% of disease chromosomes, is a 1.02 kb genomic deletion comprising exons 7 and 8, resulting in a frameshift in the coding sequence and a premature stop codon [23,33]. In mammals, CLN3 is ubiquitously expressed at a low level [24,34]. The low expression level, its hydrophobic nature and the unavailability of highly specific antibodies restricted analysis of CLN3 and so far, its function remains elusive. However, the protein presents a canonical functional lysosomal targeting motif, and prominent lysosomal localization seems most likely [34–39]. Studies from a CLN3 disease knock-in mouse model and from a resultant cell line suggest alterations in the endosomal and autophagy-lysosome system [40–42]. Other cellular studies support endosomal-lysosomal associated functions of CLN3 [43,44], altered lysosomal arginine transport in patient-derived lymphoblasts [45], and defects in Mannose-6-Phosphate receptor targeting after *CLN3* knockdown [46].

Here, we identified an interaction of PSENEN and CLN3 and demonstrated a co-distribution of transcripts as well as colocalization and cotransport of the proteins. We hypothesized that CLN3 modulates γ-secretase activity and that PSENEN and CLN3 play associated roles in the autophagy-lysosome system. To address these hypotheses, we generated isogenic *PSENEN*- and *CLN3*-deficient HeLa cell lines and confirmed impaired γ-secretase activity in the *PSENEN* knockout (KO) cells. In contrast, *CLN3* ablation did not alter γ-secretase activity to a significant degree. Additional phenotypic characterization revealed shared alterations in the autophagy-lysosome system of both KO cell lines.

Results

To identify PSENEN interaction partners, we performed a directed proteomic survey employing the tandem affinity purification (TAP) – tandem mass spectrometry methodology [47]. PSENEN was expressed with a C-terminal TAP-Tag in SK-N-BE neuroblastoma cells and subjected to tandem affinity purification, a procedure consisting of two specific binding and two specific elution steps under mild conditions, which preserve the integrity of protein-protein interactions. Affinity-purified complexes were resolved on SDS-PAGE, Coomassie-stained and co-purified proteins identified by peptide sequencing using tandem mass spectrometry. We identified CLN3 as an interaction partner and validated the interaction by co-immunoprecipitation (Figure 1A). We transfected HeLa cells with GFP-PSENEN and HA-CLN3 or GFP and HA-CLN3 and precipitated proteins with anti-GFP nanobodies. GFP-PSENEN co-precipitated HA-CLN3 whereas GFP alone was unproductive in this assay
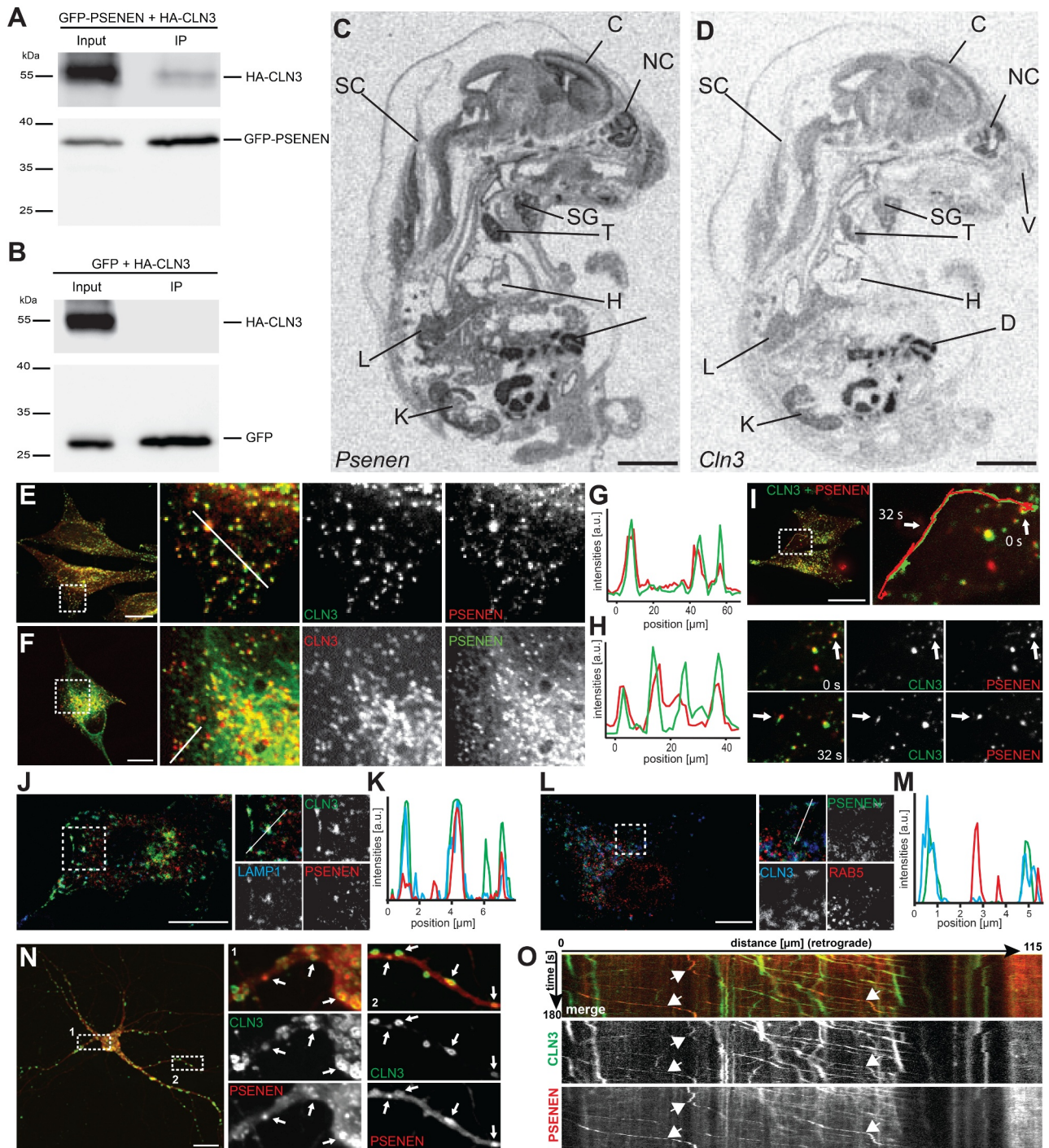
Figure 1. Interaction, co-expression and colocalization of PSENEN and CLN3. (A, B) Co-immunoprecipitation of GFP-PSENEN and HA-CLN3. GFP-PSENEN (A) or GFP (B) were co-expressed with HA-CLN3 in HeLa cells and immunoprecipitated with an anti-GFP antibody. HA-CLN3 was co-precipitated with GFP-PSENEN (**A**), but not with GFP alone (**B**). (C, D) Autoradiograms of parasagittal sections through embryonic mice at E16 hybridized with specific radiolabeled probes for *Psenen* (C) and *Cln3* (D) reveal similar expression patterns. (E, F) HeLa cells co-transfected with GFP-CLN3 (green) and tdTomato-PSENEN (red) (E) or with mCherry-CLN3 (red) and GFP-PSENEN (green) (F), were immunostained using respective antibodies and analyzed by confocal microscopy. Dotted boxes in the left panels indicate magnified areas shown in the right panels. Line plots (G, H) correspond to the white lines indicated in the merged zoom-ins in (**E**) and (**F**). (I) Tracking of GFP-CLN3- and tdTomato-PSENEN-positive endosomes in HeLa cells by time-lapse analysis using confocal spinning disk microscopy. The dotted box in the overview indicates the magnified area in which co-trafficking was analyzed. Single images below show initial position (0 s) and after tracking (32 s) of an endosome (arrows). (J, L) HeLa cells co-transfected with GFP-CLN3 and mCherry-PSENEN and immunostained using respective antibodies and an anti-LAMP1 antibody (J) or transfected with GFP-PSENEN and HA-CLN3 and immunostained using respective antibodies and an anti-RAB5 antibody (L). Dotted boxes in the left panels indicate magnified areas shown to the right. Line plots (K, M) correspond to the white lines indicated in the merged zoom-ins in (**J**) and (**L**). (N) Dissociated hippocampal neurons transfected with GFP-CLN3 (green) and tdTomato-PSENEN (red) immunostained at DIV10. Magnifications of a somatic (dotted box 1) and of a neuritic area (dotted box 2) are shown. Arrows point at areas of colocalization. (O) Time-lapse video microscopy analysis of dissociated hippocampal neurons (DIV 6) transfected with GFP-CLN3 (green) and tdTomato-PSENEN (red) imaged over 180 s. Kymographs show predominant retrograde movement of GFP-CLN3- and tdTomato-PSENEN-positive endosomes. Scale bars in (**C**) and (**D**): 2 mm; in (**E, F, I, J, L, N**): 20 μm. C, cerebral cortex; D, duodenum; H, heart; K, kidney; L, lung; NC, nasal cavity; SC, spinal cord; SG submandibular gland; T, thymus; V, vibrissae.

(Figure 1A, B). Next, we analyzed tissue expression of both genes and the subcellular localization and transport of the proteins to estimate the relevance of the observed interaction. An almost ubiquitous expression was detected in embryonic mice for *Psenen* and *Cln3* mRNA by *in situ* hybridization (Figure 1C, D). Both genes share the highest transcript levels in the gastrointestinal tract, kidney, liver, heart, thymus, and the central nervous system with prominent signals in the cerebral cortex and thalamic area. We expressed fluorophore-tagged versions of PSENEN and CLN3 in HeLa cells and in dissociated primary murine hippocampal neurons. In HeLa cells, both CLN3 and PSENEN localized to endosomal structures (Figure 1E-H). Furthermore, PSENEN and CLN3 colocalized to identical vesicles, and time-lapse video microscopy analysis demonstrated vesicular cotransport (Figure 1I and S1A). PSENEN- and CLN3-positive endosomes were to a large extend also positive for the late endosome-lysosome marker proteins LAMP1 and RAB7A, but only to a minor extend for the early endosomal marker protein RAB5A (Figure 1J-M and S1B). In neurites, PSENEN and CLN3 also colocalized to identical vesicles and the majority of PSENEN- and CLN3-positive vesicles showed a retrograde movement (Figure 1N, O). The interaction, co-expression, colocalization, and cotransport suggested an association of PSENEN and CLN3. We hypothesized that CLN3 modulates the proteolytic function of γ-secretase, because PSENEN is a subunit of the γ-secretase complex. In addition, we considered an associated role of PSENEN and CLN3 in the autophagy-lysosome system in which CLN3 is thought to play a role and PSENEN has not been studied yet.

In order to test these hypotheses, we generated *PSENEN*- as well as *CLN3*-deficient isogenic HeLa cell lines. Toward this end, we applied the CRISPR gene-editing approach and obtained independent isogenic HeLa knockout (KO) cell lines for *PSENEN* and *CLN3*. The introduced indel mutations resulted in frameshifts shortly after the start codons, leading to premature stop codons and the encoded truncated PSENEN and CLN3 proteins are most likely nonfunctional (Figure S2). We observed an unaltered morphology of the KO cells as compared to wild type cells. Proliferation of *CLN3* KO and *PSENEN* KO cells was moderately but significantly increased as compared to wild types (Figure S3).

It has been demonstrated before that PSENEN ablation impedes PSEN endoproteolytic activation, γ-secretase complex formation, and trafficking from the ER to the Golgi [2,48–50]. We analyzed the effect of PSENEN and CLN3 ablation on the intracellular localization of PSEN2 (Figure 2A). For immunocytochemical localization, we used an antibody that specifically detects the PSEN2 C-terminal fragment of proteolytically activated PSEN2 (PSEN2-CTF). In HeLa wild type and *CLN3* KO cells PSEN2-CTF is localized to endosomal structures, which are to a large extent positive for the late endosome-lysosome marker LAMP2. In contrast, employing the same PSEN2 antibody on *PSENEN* KO cells resulted in a weaker and diffuse staining (Figure 2A). We assessed the endoproteolytic processing of PSEN1 and PSEN2 by immunoblotting using C-terminal fragment specific antibodies. In wild type and *CLN3* KO cell lysates, the respective endoproteolytically-derived C-terminal fragments

were detected (Figure 2B). These were absent in cell lysates from *PSENEN* KO cells suggesting a strong reduction or the complete loss of PSEN endoproteolytic activation (Figure 2B). Next, we generated tagged γ-secretase substrates to test if *CLN3* ablation impedes or alters γ-secretase activity. We transfected cells with a Notch-ΔE HA-tagged construct that serves as a substrate for γ-secretase without prior processing by α-secretase or BACE/β-secretase [51] (Figure 2C). In alternative experiments, we used a construct encoding full-length APP (APP-FL) with a C-terminal GFP-tag (Figure 2D). The APP-FL-GFP is first cleaved by α- or BACE/β-secretase. Subsequently, γ-secretase cleavage releases the C-terminal APP-intracellular domain (APP-ICD) into the cytosol (Figure 2D). Both constructs, NOTCH-ΔE-HA and APP-FL-GFP, were processed in wild type and *CLN3* KO cells by γ-secretase, because we detected in immunoblots tagged fragments corresponding in their size to the respective intracellular domains (ICDs) (Figure 2E, G). In lysates of *PSENEN* KO cells, these fragments were absent (Figure 2E, G). In addition, immunoblot analysis of APP-FL-GFP transfected cells revealed increased levels of a larger fragment corresponding to the expected size of the transmembrane stub in *PSENEN* KO cell lysates (Figure 2G). These results demonstrate, as expected, impaired γ-secretase activity in *PSENEN* KO cells. In rescue experiments, γ-secretase activity was restored in *PSENEN* KO cells by expression of GFP-PSENEN (Figure 2F) or expression of HA-PSENEN (Figure 2H). In view of these results obtained by overexpressing γ-secretase substrates, we next assessed the processing of endogenous APP. Endogenous sAPP-α levels were almost identical between the cell lines. We measured endogenous Aβ40 and Aβ42 levels in cell culture media of wild type and knockout cells. As expected, Aβ levels were markedly reduced in *PSENEN* KO cells, whereas in *CLN3* KO cells, total Aβ levels were not significantly altered as compared to wild type cells (Figure 2I). Taken together, these experiments substantiate highly reduced or absent PSEN endoproteolytic processing and γ-secretase activity in *PSENEN* KO cells and corroborate studies by others demonstrating that PSENEN is indispensable for γ-secretase activity. In addition, the rescue experiments confirm the specificity of the *PSENEN* KO. Conversely, PSEN endoproteolytic processing and γ-secretase activity were not altered in *CLN3* KO cells strongly suggesting that CLN3 is dispensable for γ-secretase function and does not modulate its activity to a significant degree.

We reasoned that both proteins might play cooperative or converging roles in the autophagy-lysosome system. To assess lysosomal function, we compared the lysosomal-proteolytic activity of the KO cells and wild types. First, the activity of the lysosomal enzyme HEXA/β-hexosaminidase A was determined in whole cell lysates. Equal amounts of total protein from each lysate were incubated with the artificial HEXA substrate 4-nitrophenyl-N-acetyl-β-D-glucosaminide and the yield of substrate conversion to 4-nitrophenol was analyzed by spectrophotometry. As compared to wild types HEXA activity was significantly reduced in *CLN3* KO and *PSENEN* KO cells (Figure 3A). Next, we loaded cells with fluorescently labeled self-quenched polymeric bovine serum albumin (dye-quenched BSA, DQ-BSA). Upon uptake by endocytosis DQ-
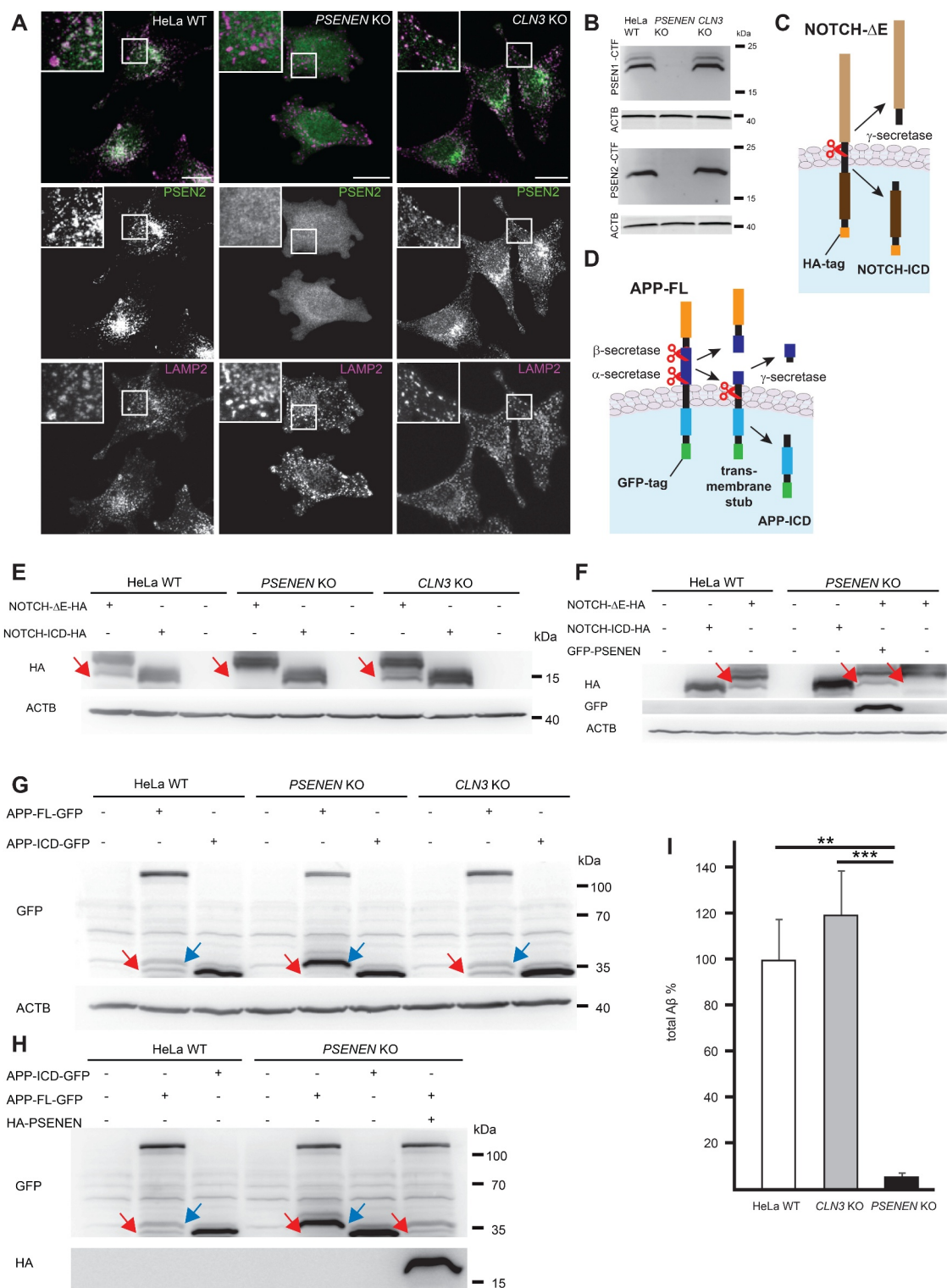
Figure 2. Impeded γ-secretase processing in *PSENEN* KO cells, but not in *CLN3* KO cells. (A) Immunocytochemical localization of PSEN2 using an antibody specific for the processed C-terminal fragment (CTF) of PSEN2 (green) and an antibody against LAMP2 (magenta) in HeLa wild type (WT), *PSENEN* KO and *CLN3* KO cells. Scale bars: 20 μm. (B) Detection of processed PSEN1 and PSEN2 in cell lysates using CTF specific antibodies. The CTFs are not detectable on immunoblots of *PSENEN* KO cell lysates indicating that PSENs are not processed. ACTB/β-actin immunoblotting was performed to control equal loading. (C) Illustration of the HA-tagged NOTCH-ΔE construct which serves as a substrate for γ-secretase without prior processing by other secretases. (D) Illustration of the GFP-tagged APP-full length (APP-FL) construct processed by α- or BACE/β-secretase before the remaining transmembrane stub is cleaved by γ-secretase and the intracellular domain (ICD) is released. (E) Analysis of cleavage products by immunoblotting. NOTCH-ICD-HA was transfected to estimate the size of the cleaved ICD. The NOTCH-ICD band is absent in *PSENEN* KO cell lysates expressing NOTCH-ΔE, but present in both WT and *CLN3* KO cell lysates (red arrows). (F) Expression of GFP-PSENEN restores γ-secretase activity in *PSENEN* KO cells. Note the presence of the NOTCH-ICD band (red arrows) in GFP-PSENEN transfectants. (G) Immunoblot analysis of APP-FL-GFP transfected cells. The band corresponding to the APP-ICD-GFP fragment is present in WT and *CLN3* KO cell lysates (red arrow). In contrast, this band is absent in *PSENEN* KO cell lysates, but levels of a larger fragment corresponding to the expected size of the transmembrane stub (blue arrows) are increased. (H) Expression of HA-PSENEN restores γ-secretase activity in *PSENEN* KO cells. Note, the presence of the APP-ICD-GFP band (red arrows) and the reduction of the band corresponding to the transmembrane stub (blue arrows) in HA-PSENEN transfectants. (I) Quantification of secreted total Aβ (Aβ40 and Aβ42) by ELISA. Aβ levels were normalized to sAPP-α levels. Data represent mean ± standard deviation (SD), one-way ANOVA p-values, **p < 0.001; ***p < 0.0001.
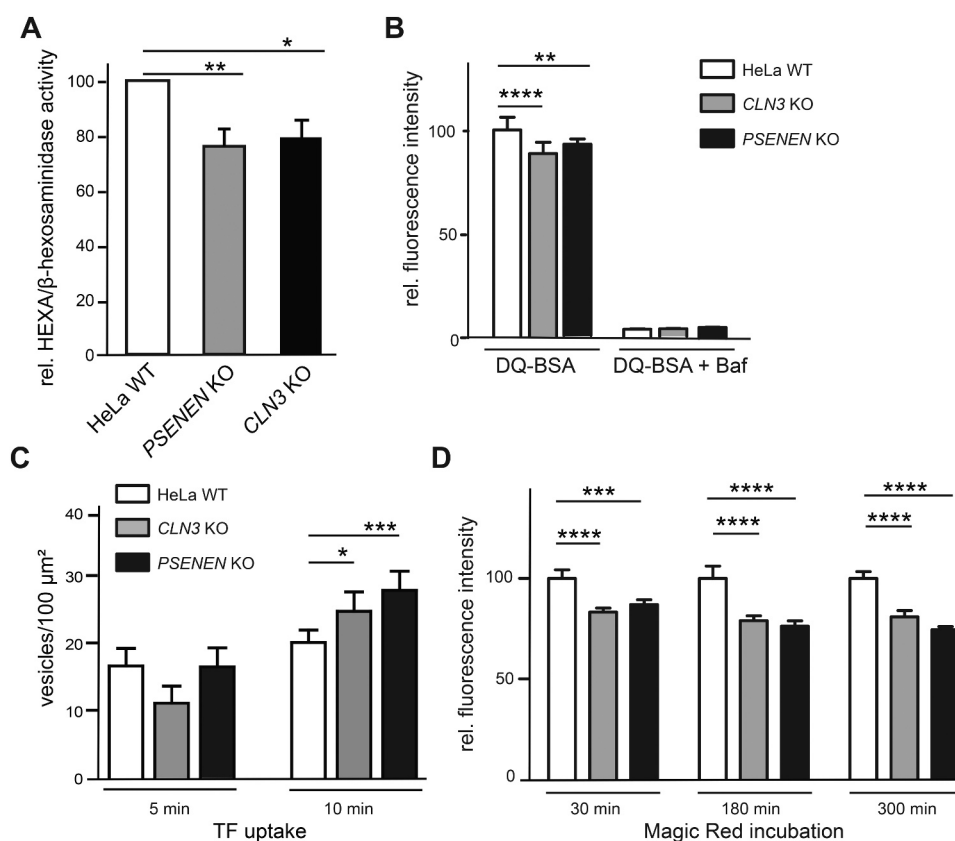
Figure 3. Ablation of *PSENEN* and *CLN3* reduces lysosomal proteolytic activity. (A) Relative activity of HEXA/β-hexosaminidase A in extracts of HeLa WT, *PSENEN* KO, *CLN3* KO cells. Data represent mean ± SD, one-way ANOVA p-values, *p < 0.05; **p < 0.001. (B) Decreased lysosomal capacity assessed through the DQ-BSA assay. Relative fluorescence intensity after 6 h incubation, with and without 100 nM bafilomycin A$_1$ (Baf) is shown. Data represent mean ± SD; two-way ANOVA p-values, **p < 0.001; ***p < 0.0001. (C) Quantification of TF uptake. Plots represent TF-Alexa Fluor 555-positive vesicles per 100 µm^2 after 5 and 10 min uptake. Data represent mean ± SD; two-way ANOVA p-values, *p < 0.05; ***p < 0.0001. (D) Lysosomal CTSB enzyme activity in HeLa WT, *PSENEN* KO, *CLN3* KO cells. Plots represent fluorescence intensity after 30 min, 180 min and 300 min of Magic Red incubation. Data represent mean ± SD; two-way ANOVA p-values, ***p < 0.0001; ****p < 0.00001.

BSA accumulates in lysosomes. As DQ-BSA enters these acidic compartments, proteases cleave the polypeptide and generate fluorescent peptide fragments. The rate of the released fluorescence increases proportionally to the activity of the lysosomal proteases. A lower rate of DQ-BSA hydrolysis suggests a decrease in the activity of lysosomal proteases *in situ*. Fluorescence intensity was monitored and compared in the presence or absence of bafilomycin A$_1$. Bafilomycin A$_1$ is inhibiting vacuolar-type H$^+$-ATPase (V-ATPase)-dependent acidification of lysosomes. A significant reduction of fluorescence intensity was detected in *CLN3* KO and *PSENEN* KO cells as compared to WT cells (Figure 3B and S4A). Pre-incubation with bafilomycin A$_1$ resulted in a distinct decrease of fluorescence signals in all investigated cell lines. To exclude that the DQ-BSA results were obscured by differential endocytic uptake by the KO versus wild type cells, we performed a TF (transferrin)-uptake experiment. Cells were labeled on ice with TF conjugated to a fluorescent dye. After washing, cells were incubated at 37°C for different time points and fluorescent vesicles were determined. TF uptake was comparable after 5 minutes and slightly increased after 10 min in the two KO cell lines as compared to wild types confirming that endocytic uptake rates were not a limiting factor (Figure 3C and S4B). In addition, we engaged the Magic Red Cathepsin B assay. This

fluorescence based live cell assay employs a cell membrane permeant substrate and, therefore, cannot be affected by possible differential endocytosis rates. The substrate is cleaved upon cathepsin enzyme activity in lysosomes and results in a fluorescent signal. Fluorescence intensity was monitored and compared at three time points, after 30 min, 180 min and 300 min substrate incubation. *CLN3* KO and *PSENEN* KO cells showed significantly lower fluorescence intensities as compared to isogenic wild types for all three incubation times (Figure 3D and S4C). Taken together, three assays independently confirmed a decreased lysosomal activity in both KO cell lines.

To further investigate the impact of *PSENEN* or *CLN3* ablation on the endosomal-lysosomal system, we assessed changes in the subcellular localization of endosomal markers in KO and wild type cells. To this end, we analyzed the relative overlap of the late endosomal/lysosomal proteins LAMP1 and LAMP2 with the early endosomal marker protein RAB5 and the retromer subunit VPS35 which is crucial for retrieval and recycling from early endosomes to the trans Golgi network or the plasma membrane. In all cell types, RAB5 or VPS35 displayed no enhanced localization to LAMP1- or LAMP2-positive structures under control conditions or after starvation (Figure 4A and S5). RAB9 has been involved in retrograde transport from late endosomes to
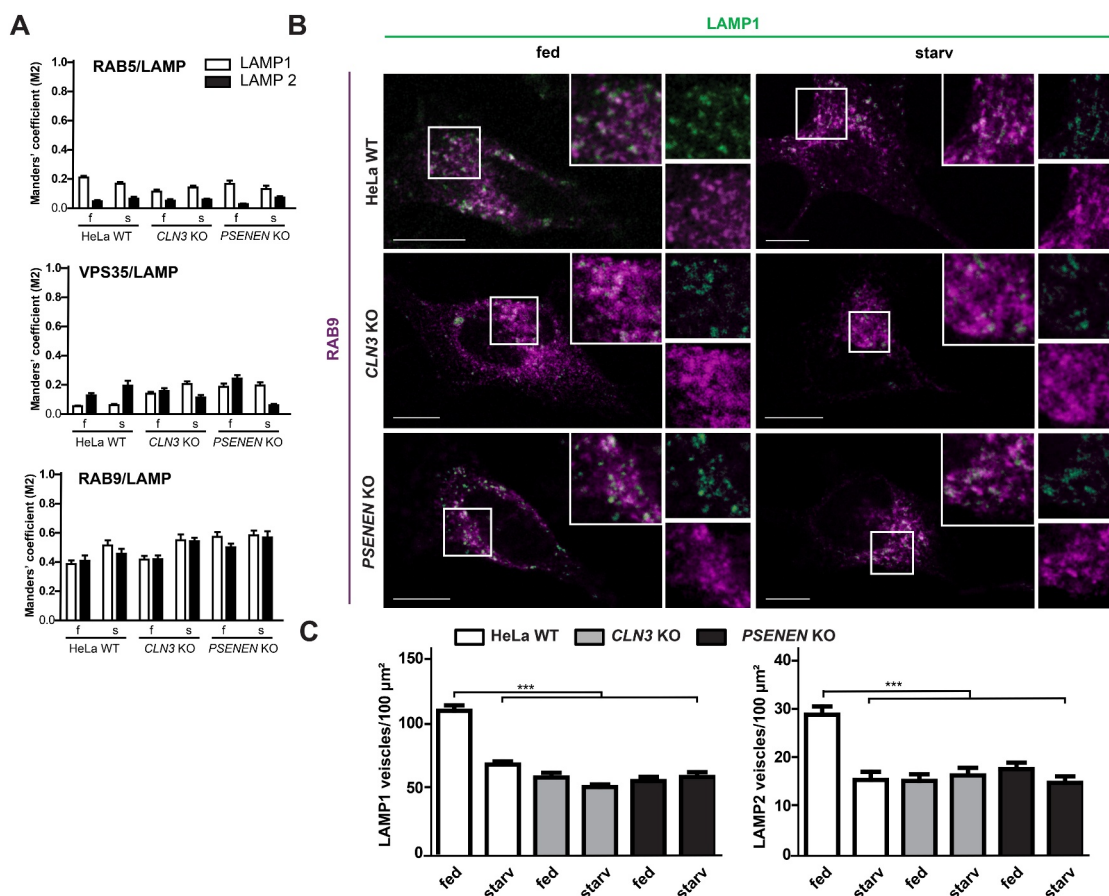
Figure 4. Ablation of *PSENEN* and *CLN3* reduces the number of lysosomes. (A) Plots show the Manders' coefficient of LAMP1 or LAMP2 immunocytochemical co-localization with RAB5, VPS35 and RAB9 in fed HeLa WT, *CLN3* KO, *PSENEN* KO cells and after 6 h starvation (S). Values are means ± SD of n = 50 cells pooled from three different experiments. (B) Representative confocal images of LAMP1 (green) and RAB9 (magenta) immunocytochemical localization in fed HeLa WT, *CLN3* KO, *PSENEN* KO cells and after 6 h starvation (starv). Scale bars: 10 μm. (C) Plots represent LAMP1- and LAMP2-positive vesicles per 100 μm². Values are means ± SD of n = 50 cells pooled from three different experiments; one-way ANOVA p-values, ***p < 0.0001.

lysosomes, in the targeting of lysosomal enzymes and mannose-6-phosphate receptors and is suggested to play a role in autophagosome biogenesis [52]. In fed wild type cells we observed colocalization of RAB9 with LAMP1 and LAMP2. This was slightly increased in starved cells. In *PSENEN* KO cells and in *CLN3* KO cells, localization of RAB9 to LAMP1- and LAMP2-positive vesicles was further increased after starvation, suggesting minor alterations in Golgi to late endosome-lysosome compartmentalization (Figure 4A, B). Quantification of LAMP1- and LAMP2-stained vesicles revealed a significantly reduced number in starved wild type cells as compared to fed cells (Figure 4C). We observed already in fed *PSENEN* KO and *CLN3* KO cells a reduction of LAMP1- and LAMP2-positive vesicles to the same degree as shown in starved wild type cells (Figure 4C). After starvation, the number of LAMP1- and LAMP2-stained endosomes was not further decreased in the KO cells (Figure 4C). Taken together, these experiments demonstrate reduced lysosomal proteolytic activity and a reduced number of late endosomes-lysosomes in both KO cell lines.

We assessed as well the localization of the autophagosome marker LC3 to LAMP1- and LAMP2-positive structures. In all 3 cell lines we observed only minor localization of LC3 to LAMP1- and LAMP2-positive vesicles under control (fed) conditions (Figure 5A and S6). Starvation moderately expanded the localization of LC3 to these structures. This was even more evident after treatment with the lysosomotropic chemical ammonium chloride (NH₄Cl) that neutralizes lysosomal pH, prevents the fusion of autophagosomes with lysosomes and promotes aggregation of autophagosomes (Figure 5A and S6). However, these immunocytochemical analyses did not reveal obvious differences between the cell lines. Subsequently, we employed immunoblotting to monitor LC3 levels. LC3 is a microtubule-associated protein playing an important role in autophagosome formation. After initial synthesis, LC3 is proteolytically processed, named LC3-I, and finally lipidated, named LC3-II. The latter is associated with autophagosomal membranes and detectable by immunoblotting [53]. To assess alterations of LC3-II levels in the isogenic cell lines, we quantified these in immunoblots of cell lysates. Control cells were compared with cells treated with NH₄Cl alone or together with lysosomal inhibitors. We already observed a small increase of the LC3-II:ACTB/β-actin ratio in *PSENEN* KO and *CLN3* KO cells as compared to wild types under control conditions (Figure 5B,C). This difference was more pronounced after the addition of NH₄Cl alone or in combination with the lysosomal protease inhibitors E64d and pepstatin A (Figure 5B,C). In independent experiments, we
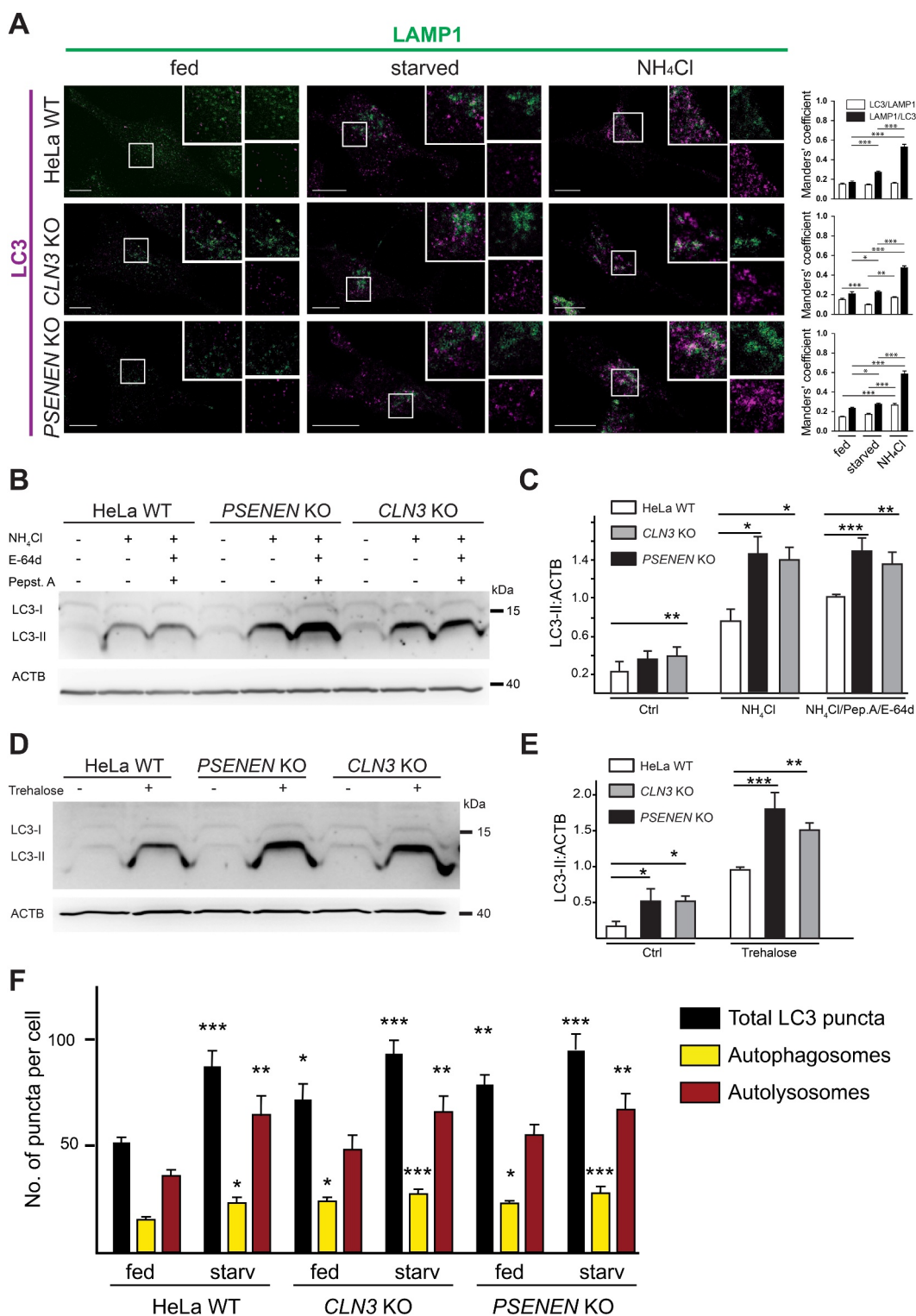
Figure 5. Altered LC3-II levels and autophagy induction in *PSENEN* KO and *CLN3* KO cells. (A) Representative confocal images of LAMP1 (green) and LC3 (magenta) immunocytochemical localization in fed HeLa WT, *CLN3* KO, *PSENEN* KO cells, 6 h after starvation or 6 h after NH_4Cl treatment. Scale bars: 10 μm. Plots on the right show respective Manders' coefficient of LAMP1 and LC3 co-localization. Values are means ± SD of n = 50 cells pooled from three different experiments. (B) Representative immunoblot analysis of endogenous LC3 (LC3-I and -II) and ACTB under control conditions or after NH_4Cl alone or together with lysosomal inhibitor treatment for 6 h. (C) Densiometric analysis of LC3-II band intensity normalized to ACTB. Values are means ± SD of n = 10 independent experiments; one-way ANOVA with Dunnett's post hoc test. (D) Representative immunoblot analysis of endogenous LC3 (LC3-I and -II) and ACTB under control conditions or 24 h after trehalose treatment. (E) Densiometric analysis of LC3-II band intensity normalized to ACTB. Values are means ± SD of n = 7 independent experiments; one-way ANOVA with a Dunnett's post hoc test. (F) HeLa WT, *CLN3* KO or *PSENEN* KO cells were transfected with a mCherry-GFP-LC3 construct, cultured under control conditions (fed) or starved for 6 h in EBSS (starv) and analyzed by live confocal microscopy. The plots show the quantification of total LC3-positive puncta (black), the number of autophagosomes (spots positive for GFP and positive for mCherry) (yellow) and number of autolysosomes (spots negative for GFP and positive for mCherry) (red). Values are means ± SD of n = 3 independent experiments. Total numbers of LC3 puncta per cell, autophagosomes per cell and autolysosomes per cell in starved WT cells and in fed or starved KO cells were compared to the respective numbers in fed WT cells. p-Values were calculated using one-way ANOVA with a post hoc Tukey test, *p < 0.05; **p < 0.001; ***p < 0.0001.

applied trehalose, which is regarded as a mTORC1-independent autophagy enhancer [53]. Consistently, we also observed under control conditions a small increase of the LC3-II:ACTB ratio in PSENEN KO and CLN3 KO cells. Trehalose treatment further increased the LC3-II:ACTB ratio (Figure 5D,E). Collectively these data suggested increased autophagosome levels in the KO cells. These could be caused by a block of the autophagic flux due to hampered lysosome-autophagosome fusion or by enhanced autophagosome biogenesis.

To assess the autophagosome-lysosome fusion, cells were transfected with a tandem fluorophore-tagged LC3 expression construct and analyzed by confocal live microscopy. LC3-II fused to both GFP and mCherry is detectable as green and red puncta at the autophagosome membrane. Upon fusion of autophagosomes with acidic lysosomes, the acid sensitive fluorescent GFP signal is quenched by low pH, whereas the acid insensitive mCherry signal is still detectable until final degradation in autolysosomes. This change in fluorescence allows visualization of the autophagic flux. The total number of LC3-II-positive puncta significantly increased in wild types after starvation (Figure 5F). In both knockout cells, the total number of LC3-II-positive puncta was already increased to a similar degree under fed conditions and further raised by starvation (Figure 5F). The increased total LC3-II puncta, which corresponds to increased LC3-II levels, observed after expression of the tandem fluorophore-tagged LC3 construct in the KO cells compared to wild types is in accordance with the elevated endogenous LC3-II levels detected in immuno-blots (Figure 5B-E). As compared to fed cells, wild type cells exhibited increased levels of autophagosomes (yellow, overlay of red, mCherry, and green, GFP, puncta) and autolysosomes (red puncta) after 6 h starvation (Figure 5F and S7). Already in fed KO cells, the number of autophagosomes and autolysosomes was elevated compared to wild type cells and further increased by starvation (Figure 5F). In all three cell types, the number of autolysosomes was higher than the number of autophagosomes and both increased after starvation. This strongly suggests a functional fusion of autophagosomes and lysosomes in all cell types.

In summary, these observations demonstrate an increased number of autophagosomes and an increased fusion of autophagosomes and lysosomes in the KO cells. This prompted us to investigate altered lysosome and autophagosome biogenesis on the transcriptional level. The expression of lysosomal and autophagic genes in response to pathways sensing lysosomal stress and nutritional conditions is coordinated to a large extent by TFEB (transcription factor EB) [54]. To assess the altered transcription of lysosomal/autophagy genes by TFEB, we monitored the expression of a number of TFEB target genes and genes encoding lysosomal proteins under control conditions and 2 h, 4 h, 6 h, or 8 h after starvation by quantitative real-time PCR (RT-qPCR) (Figure 6). In this expression analysis, we included the knocked-out genes CLN3 and PSENEN. In the knockout cells, the non-coding transcripts of the respective knocked-out genes (Figure S2) were detected, but their expression was markedly reduced (Figure 6). In CLN3 KO cells, PSENEN transcript levels were almost unchanged, but slightly induced 2 and 4 h after

starvation. In PSENEN-KO cells, CLN3 expression was moderately but constantly upregulated at all analyzed time points. PSEN2 expression was increased in PSENEN KO cells with strongest induction after 4 h starvation. TFEB expression was upregulated in fed and starved CLN3 KO cells with maximal expression 4 h after starvation. This expression peak was shared by PSENEN KO cells. Transcript levels of other lysosomal proteins such as CTSB (cathepsin B) and CTSD (cathepsin B), GLB1/β-galactosidase (galactosidase beta 1), PSAP (prosaposin), and TPP1, as well as SESN2 (sestrin 2) were upregulated in fed and starved PSENEN KO cells. In CLN3 KO cells these transcript levels were not always altered, but in most cases upregulated after 4 h starvation. These results demonstrate an overall increased expression of TFEB targets (CTSB, CTSD, GLB1, PSAP, TPP1) and of TFEB itself in fed and starved PSENEN KO. Notably, expression of SESN2, which is not regarded as a TFEB target [55], was induced similarly and suggested the involvement of additional factors. In fed and starved CLN3 KO cells, however, TFEB expression was upregulated and transcript levels of some lysosomal genes were increased after 4 h starvation. Since both knockouts affected expression of TFEB or TFEB regulated target genes, we investigated TFEB in more detail. TFEB localizes to the cytosol. Upon activation, it translocates to the nucleus and initiates gene expression. Next, we assessed altered nuclear versus cytosolic localization of TFEB by immunocytochemistry. Nuclear localization was slightly increased in fed KO cells as compared to wild types and this difference was more pronounced after 2 h and 4 h starvation (Figure 7). However, after 6 h starvation a comparable nuclear localization of TFEB was observed in wild type and KO cells (Figure 7 and S8). Finally, we analyzed TFEB protein levels by immunoblotting and observed increased TFEB levels in both KO cell lines (Figure 8A). Starvation induces dephosphorylation of TFEB, which corresponds to a reduced molecular weight observed in immunoblots (Figure 8A). Stable expression of GFP-PSENEN in PSENEN KO cells and of CLN3 in CLN3 KO cells, respectively, reversed the increased TFEB levels (Figure 8B,C). Taken together, these analyses demonstrate increased TFEB levels following PSENEN as well as CLN3 ablation and strongly suggest altered activity of TFEB in the analyzed PSENEN KO and CLN3 KO HeLa cell lines.

Discussion

We identified an interaction of PSENEN and CLN3 and demonstrated co-expression, colocalization, and endosomal cotransport of both proteins. Mutations in the respective genes are causative for different neurodegenerative diseases, AD and CLN3 disease. Therefore, understanding the shared cellular function of both proteins might be pertinent for understanding general cellular mechanisms underlying neurodegenerative diseases. To investigate the relation of PSENEN and CLN3 on a cellular level, we generated isogenic knockout HeLa cell lines.

PSENEN is a subunit of the γ-secretase complex. Accordingly, we hypothesized that CLN3 might alter γ-secretase function and studied γ-secretase mediated processing in the KO cells. In accordance with previous
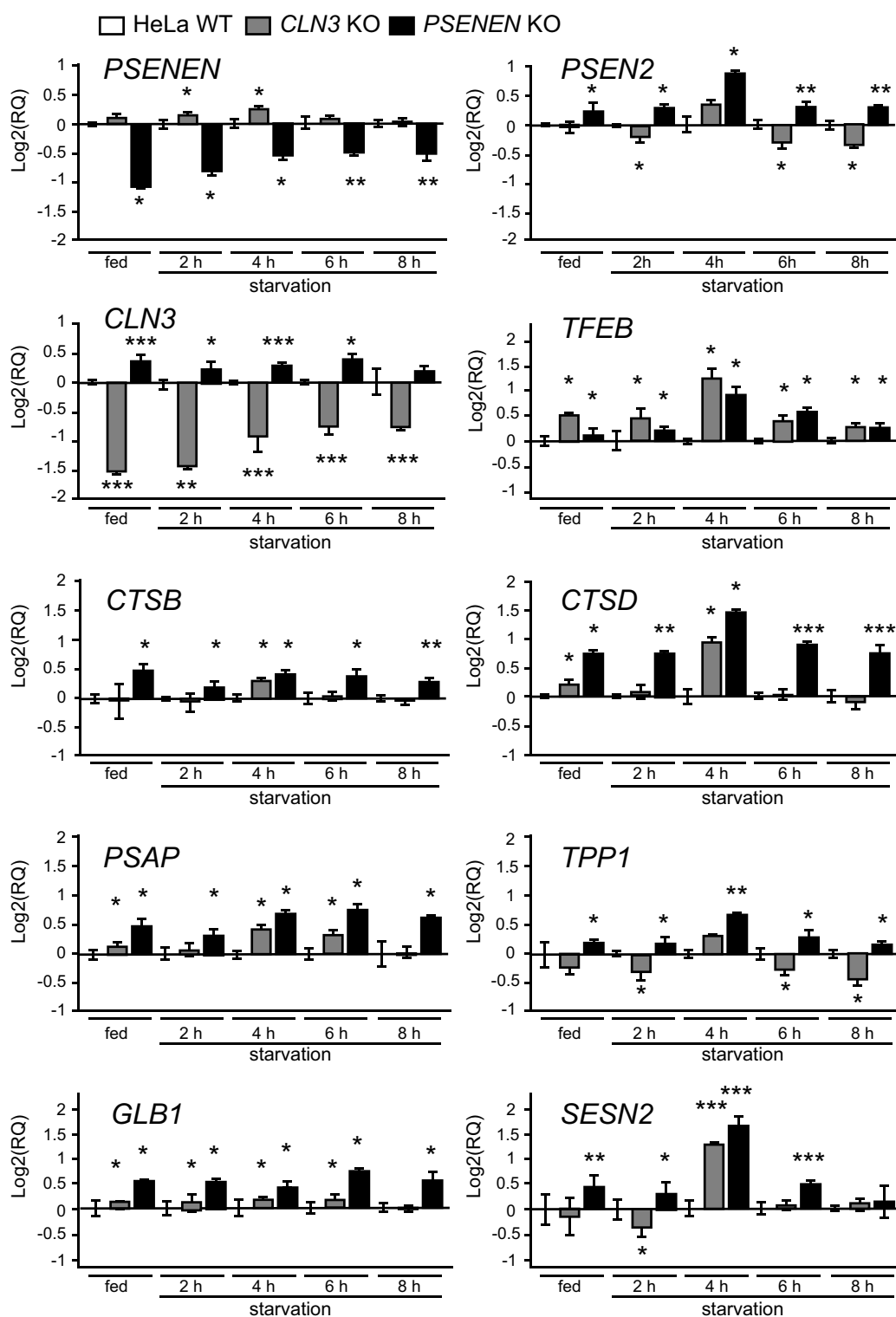
Figure 6. Gene expression analysis of *PSENEN* KO and *CLN3* KO cells. *APRT*-normalized mRNA changes under control conditions (fed) and 2 h, 4 h, 6 h and 8 h after starvation analyzed by real-time qPCR. Changes were normalized to wild type cells. The experiment was repeated with *HPRT*-normalization and similar results obtained. RQ, mean expression level; mean ± SD. p-Values were calculated using REST©-software, *p < 0.05; **p < 0.001; ***p < 0.0001.

studies, we demonstrate that PSENEN is essential for forming a functional γ-secretase complex and is indispensable for γ-secretase activity. Whereas the knockout of *Psenen* in mice results in an embryonic lethal phenotype [50], its ablation appears not per se mortal on a cellular

level. This corroborates the notion that inhibition or knockout of γ-secretase does not generally lead to toxicity in cell culture, suggesting that general removal of protein stubs is not essential or that other means of removal exist [7].
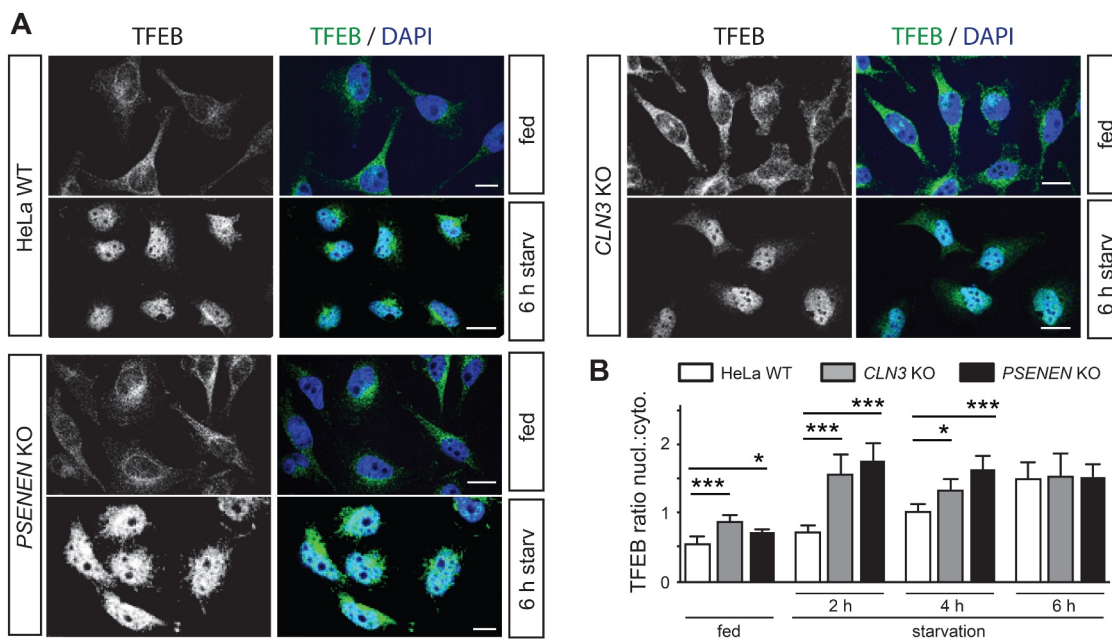
Figure 7. Accelerated TFEB nuclear translocation in *PSENEN* KO and *CLN3* KO cells. (A) Images of TFEB (green) immunolocalization in HeLa WT, *CLN3* KO and *PSENEN* KO cells under control conditions (fed) and 6 h after starvation (6 h starv). DAPI (blue) was used to label nuclei. Scale bars: 10 μm. (B) Plots show the TFEB nuclear to cytosolic ratio under control conditions and 2 h, 4 h and 6 h after starvation. Values are means ± SD of n = 20 cells pooled from three independent experiments, one-way ANOVA with a post hoc Tukey test *p < 0.05; ***p < 0.0001.
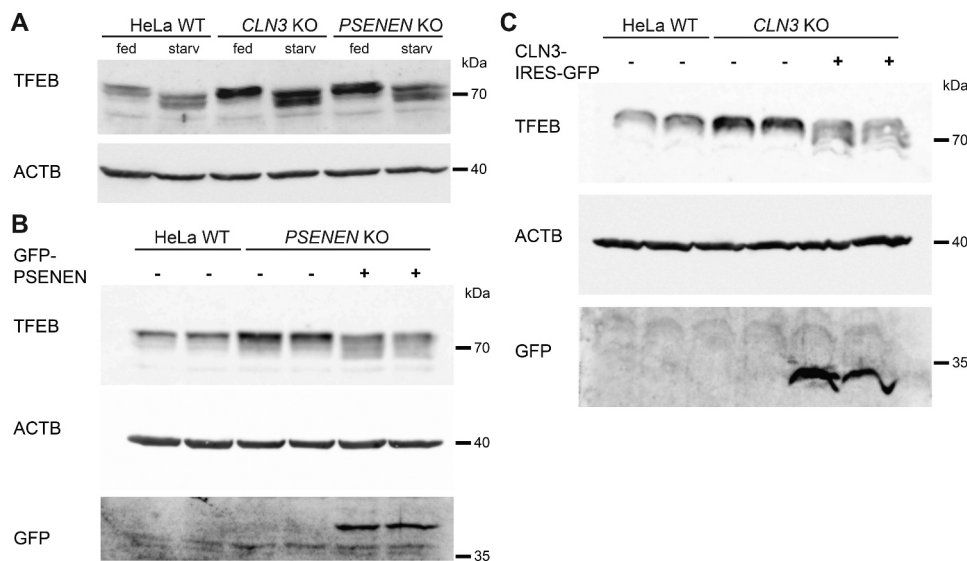

Figure 8. Increased TFEB levels in *PSENEN* KO and *CLN3* KO cells. (A) Immunoblot analysis of TFEB in HeLa wild type (WT), *CLN3* KO and *PSENEN* KO cells under control conditions (fed) and after 3 h starvation (starv). ACTB levels are shown as loading controls. (B) Elevated TFEB levels under control conditions in *PSENEN* KO cells were reduced to wild type levels when stably transfected with GFP-PSENEN. Stable GFP-PSENEN expression was confirmed using anti-GFP antibody. Two independent cell clones were analyzed. (C) Elevated TFEB levels under control conditions in *CLN3* KO cells were reduced to wild type levels when stably transfected with CLN3. Stable expression of the CLN3-IRES-GFP construct was confirmed by anti-GFP antibody and by sequencing of RT-PCR-amplified *CLN3* transcripts. Two independent cell clones were analyzed.

We provide strong evidence that, in contrast to PSENEN, CLN3 is dispensable for γ-secretase function and does not modulate its activity to a significant degree. This implies that some of the previously described similarities in AD and CLN3 disease pathology, such as the accumulation of Aβ, are not a direct consequence of *CLN3* ablation. We cannot exclude a dominant negative role of CLN3 mutants in altering γ-secretase function. This seems, however, unlikely as the most prevalent mutation found in CLN3 disease is regarded

as a functional ablation of the CLN3 protein that, if expressed at all, is retained in the ER [34,56–58].

In agreement with its role in a lysosomal storage disease and its assumed subcellular localization, previous studies demonstrated alterations in the autophagy-lysosome system upon *CLN3* ablation. A recent study employed siRNA-mediated knock down of CLN3 and observed enhanced autophagosome biogenesis and autophagic flux [59]. In accordance with our results, this study suggests functional

lysosome and autophagosome fusion in *CLN3* ablated cells and not its impairment as described for a number of lysosomal storage diseases. Moreover, the authors proposed an enhancement of the autophagy-lysosome system as a compensatory stress response to impaired energy metabolism upon *CLN3* deficiency [59]. The upregulation of *TFEB* transcripts and an increase of *CTSB, CTSD, PSAP, TPP1* expression observed here after starvation in *CLN3* KO HeLa cells also suggests a compensatory mechanism to cope with a metabolic deficit caused by the absence of CLN3 in lysosomes.

To investigate CLN3 function, three different knockout and knock-in mouse models have been generated [60–62]. All three models resemble a number of phenotypic and histopathological abnormalities of the human CLN3 disease, including the accumulation of storage material predominantly composed of ATP5MC/subunit c of the mitochondrial ATP synthase. Therefore, a *CLN3* knockout is regarded as a disease model.

The so far most frequently used cellular model for CLN3 disease is a cerebellar neuronal precursor cell line (CbCln3 delta ex7/8 cells) derived from a CLN3 disease knock-in mouse [62]. These cells accumulate storage material, ATP5MC, in enlarged lysosomes [41,42]. This occurred in confluent cells, but not under sub-confluent conditions [42]. Moreover, under sub-confluent conditions the number of lysosomes was reduced [63], whereas the number of autophagosomes was increased [64]. The observations in sub-confluent cells corroborate our results in HeLa *CLN3* KO cells, reduced number of lysosomes and increased numbers of autophagosomes. Notably, we failed to observe the accumulation of storage material in HeLa *CLN3* KO cells when we analyzed ATP5MC levels at steady state and after cell cycle arrest. Thus, it is tempting to speculate that the here generated HeLa *CLN3* KO cells correspond to cells that are still capable adapting to several of the gene ablation-initiated defects before developing disease-like cytopathology. The observed increased TFEB levels might counteract disease-like progression, such as the accumulation of storage material.

TFEB coordinates the expression of lysosomal and autophagic genes in response to pathways sensing lysosomal stress and nutritional conditions. Thus, the identified increased autophagosome and autolysosome levels are in accordance with increased TFEB levels. In line with these assumptions, increased TFEB levels have been shown to induce lysosomal exocytosis and to rescue pathologic intracellular storage [65]. A pharmacological activation of TFEB reversed some of the phenotypes in CLN3 disease mouse models [66]. Notably, TFEB activation has been suggested as a possible strategy to counteract disease progression in a broader range of neurodegenerative diseases [54] and mice with neuronal-targeted TFEB are characterized by reduced levels of amyloid-β peptides and amyloid plaques [67].

It is conceivable, that the here studied HeLa cells are less prone to accumulate storage material. Therefore, further studies employing more differentiated cells that possess a highly active lysosomal compartment or non-dividing cells which might more likely accumulate storage material should be used to substantiate to what extend increased TFEB levels

and other factors ameliorate pathological phenotypes on a cellular level.

A structure-based prediction in combination with additional functional clues supports the here identified interaction of PSENEN and CLN3 [68] and was specified in the integrated interactions database [69]. CLN3 has been shown to play a role in the lysosome-autophagy system before. Therefore, and irrespective of the nature of the PSENEN and CLN3 interaction, which may be transient or part of a larger complex, we speculated that PSENEN plays also a role in the lysosome-autophagy system and ablation of both proteins might result in concordant cellular phenotypes.

To the best of our knowledge, this is the first study considering PSENEN function in the endosomal-lysosomal-autophagy system, and the observed consequences of *PSENEN* ablation have not been described before. In contrast to the difference in γ-secretase function, *PSENEN* KO and *CLN3* KO cells presented indeed to a large extend corresponding alterations in our analyses. We observed in both KO cells a reduced activity of lysosomal enzymes, a reduced number of late endosomes and lysosomes, an increased number of autophagosomes and autolysosomes, and increased TFEB levels.

The autophagic flux includes autophagosome-lysosome fusion and (auto-) lysosomal degradation. Our data suggest functional and increased autophagosome-lysosome fusion in *PSENEN* KO and *CLN3* KO cells, whereas the lysosomal degradation appears reduced. The observed increased autophagosome-lysosome fusion might consume a large number of lysosomes. Along with a shortage of lysosomal degradation, lysosome recycling, or biogenesis, this might be causative for the reduced number of late endosomes and lysosomes in the KO cells.

CLN3 transcript levels were increased in *PSENEN* KO cells. This finding supports a possible compensatory upregulation of transcripts following the ablation of an interaction partner. However, *PSENEN* KO cells demonstrated increased expression of several lysosomal genes and *CLN3* induction might also be part of a general induction of lysosomal genes in *PSENEN* KO cells.

Taken together, on the cellular level the *PSENEN* KO resembles to a large extend the cellular phenotype of a knockout of the lysosomal storage disease gene *CLN3*. Autophagy impairment is commonly implicated in the pathological characteristics of AD [12]. PSENEN is a subunit of the γ-secretase complex. PSEN2 harbors a lysosomal targeting signal [21], and γ-secretase complexes including PSEN2 are targeted to lysosomes [20,21]. So far, functions in the autophagy-lysosome system have been proposed particularly for PSEN1, but how PSEN1 regulates lysosomal function remains controversial [11,15–19]. However, pharmacological γ-secretase inhibition did not alter lysosome-autophagy functions to a similar degree, suggesting that these alterations are independent of γ-secretase activity [11]. The here studied *PSENEN* knockout impairs the formation of all γ-secretase complexes, similar to a double knockout of *PSEN1* and *PSEN2* (*PSEN* dKO). Therefore, a phenotypic overlap between *PSENEN* KO and *PSEN* dKO cells is expected. Phenotypic differences might point to γ-secretase complex independent

functions of PSENEN or of PSENs. Analyses of *psen* dKO embryonic stem cells and *psen* dKO mice derived embryonic fibroblasts demonstrated increased and decreased LC3-II levels [11,19,70]. Moreover, increased TFEB protein levels, reduced nuclear translocation of TFEB after starvation and a reduced expression of TFEB target genes have been described [70]. Although some of these observations are inconsistent, a partial phenotypic overlap, such as increased LC3-II and TFEB levels, in *PSENEN* KO and *PSEN* dKO cells seems likely. However, clarification of a putative function of γ-secretase in the autophagy-lysosome system, that is independent of substrate cleavage, clearly requires additional studies on the individual γ-secretase components.

In summary, the identical alterations observed in the isogenic *PSENEN* KO and *CLN3* KO cells support γ-secretase independent function of PSENEN in the autophagy-lysosome system and our results point to dysfunctions in the autophagy-lysosome system that might in general be causative for different neurodegenerative diseases.

Materials and methods

Antibodies

The following primary antibodies were used: ACTB/β-actin (Sigma, A5441; Western blot [WB] 1:100.000); DS-red (Clontech, 632,496; immunocytochemistry [ICC], 1:500); GFP (Abcam, ab13970; ICC 1:5000, WB 1:10.000); HA-epitope-tag (Covance, MMS-101 R; WB 1:1000); LAMP1 (BD Bioscience, 555,798; ICC, 1:3000); LAMP2 (BD Bioscience, 555,803; ICC 1:3000); LC3B (Novus, NB100-2220; WB 1:1000); LC3B (clone EPR18709, Abcam, ab192890; ICC 1:3000); PSEN1 (clone EP2000Y, Abcam, ab76083; WB 1:1000); PSEN2 (clone EP1515Y, Abcam, ab51249; WB 1:1000, ICC 1:3000); RAB5 (Abcam, ab18211; ICC 1:1000); RAB9 (Cell Signaling, 5118; ICC, 1:1000); TFEB (Cell Signaling, 37,785; ICC 1:1000); TFEB (Cell Signaling, 4240; WB 1:1000); VPS35 (Abcam, ab10099; ICC 1:500). Fluorescent Alexa Fluor conjugated (Invitrogen, A11001, A11008, A11039, A21428 or A21422) or horseradish peroxidase (HRP)-conjugated (Dianova, 49,988 or 49,533) secondary antibodies were used.

DNA constructs

PSENEN-TAP was generated by site-specific recombination of a PCR-amplified ORF of PSENEN into a modified TAP-tagged version of the Moloney murine leukemia virus-based vector pZome1 (Cellzome). The TAP-tag was built of a protein A and a CALM (calmodulin)-binding site separated by a tobacco etch virus (TEV) cleavage site. Human *PSENEN* cDNA was PCR-amplified, cloned into the pENTR/D-TOPO cDNA vector (Thermo Fisher Scientific, K240020), and transferred by LR recombination using Gateway LR Clonase (Thermo Fisher Scientific, 11,791,019) into the L21 vector. L21 is available in different versions encoding N-terminal protein tags (HA, GFP, tdTomato), added in frame to the insert cloned into the Gateway cassette [34]. A corresponding portfolio of tagged CLN3 constructs has been generated by us

before [34]. In addition, human *CLN3* was PCR-amplified and cloned into pIRES2-EGFP (BD Bioscience, PT3267-5), and the CLN3-IRES2-EGFP cassette was finally transferred into pcDNA3.1/Zeo (Invitrogen, V86020). pCS2 NOTCH1 ΔEMV-6MT was a gift from Raphael Kopan and Jeffrey Nye (Addgene, 41,737) [51] and used as a template for PCR-amplification and cloning of the full-length insert or of a fragment encoding the intracellular domain respectively into pENTR/D-TOPO and subsequently into L21 to generate HA-tagged constructs. Full-length APP695 in pcDNA3.1 [71] was used as a template for PCR-amplified cloning of the full-length insert or of a fragment encoding the intracellular domain respectively into pENTR/D-TOPO and subsequently into L21 to generate GFP-tagged constructs. pBABE-puro mCherry-EGFP-LC3B was a gift from Jayanta Debnath (Addgene, 22,418) [72] and used for subcloning of mCherry-EGFP-LC3B into L21. tdTomato-RAB5A and tdTomato-RAB7A were cloned into L21 tdTomato from GFP-RAB5A and GFP-RAB7A [71] by LR recombination. pLAMP1-mCherry was a gift from Amy Palmer (Addgene, 45,147) [73].

Tandem affinity purification

Tandem affinity purification was performed as described before [47]. In brief, SK-N-BE (2) neuroblastoma cells expressing PSENEN with a C-terminal TAP-Tag were generated by retroviral gene transfer. Cell lysates were incubated with 200 μl of IgG-agarose beads (Sigma, A0919) for 2 h at 4°C. Beads were collected, washed and incubated with cleavage buffer (10 mM Tris, pH 7.5, 100 mM NaCl, 1 mM DTT, 0.1% Igepal [Sigma, I-3021], 0.5 mM EDTA) and 100 units of TEV protease (Invitrogen, 12,575,023) for 1 h at 16°C. The eluate was transferred into a column containing 200 μl of calmodulin-agarose (Stratagene, 214,303) in 10 mM Tris, pH 7.5, 100 mM NaCl, 1 mM DTT, 0.1% Igepal, 2 mM MgCl₂, 2 mM imidazole (Roth, 3899.2), 4 mM CaCl₂ and after washing bound proteins were eluted with 10 mM Tris, pH 8.0, 5 mM EGTA at 37°C. Eluates were separated by SDS PAGE and stained with colloidal Coomassie Brilliant Blue (Bio-Rad, 1,610,436). Gels were sliced, cut bands reduced, alkylated, and digested as described previously [74] and peptides were sequenced by tandem mass spectrometry (Waters Cap LC and QTOF Ultima). Proteins were identified by using Mascot software (Matrix Science, UK).

Cultivation and transfection of cells

HeLa cells (DSMZ, ACC57) were cultured in Dulbecco's modified Eagle's medium (DMEM) (Gibco, 11,971–025) supplemented with 10% fetal calf serum (FCS, GIBCO, 10,109,163). Cells were transiently transfected using Lipofectamine 2000 (Invitrogen, 11,668,019) according to the manufacturer's instructions. Stable transfectants were selected and cultured in DMEM containing 150 μg/ml Zeocin (Invivogen, ant-zn) as described previously [75]. Positive cell clones with equal expression levels were identified by immunocytochemistry and immunoblot analysis. In addition, cells expressing the GFP-IRES-CLN3 construct were

analyzed for wild type CLN3 expression by RT-PCR and sequencing of respective PCR products.

For starvation, cells were cultured for indicated times in Earle's Balanced Salt Solution (EBSS; Gibco, 24,010). To challenge the autophagy pathway, cells were cultured for 6 h in DMEM supplemented with 10 mM NH_4Cl (Sigma, 213,330) alone or with the protease inhibitors E-64d (Sigma, E8640) or pepstatin A (Applichem, A2205) (each 10 μg/ml) or for 24 h in DMEM supplemented with 100 mM trehalose (Sigma, T9531).

Primary cultured hippocampal neurons were prepared as described before [76]. In brief, we used E17 embryos from timed-pregnant C57BL/6 J mice. Dissected hippocampi were collected in HANKS' medium without calcium and magnesium (Sigma, H-2387) supplemented with 20% FCS, washed in HANKS' medium, and treated with papain (Sigma, P4762) and DNAse (Invitrogen, 18,047–019) in digestion buffer (137 mM NaCl, 5 mM KCl, 7 mM $Na_2HPO_4(2xH_2O)$, 25 mM HEPES, pH 7.4) for 30 min at 37°C. Tissue was subsequently washed two times with HANKS' medium and resuspended in 2 ml dissociation buffer (HANKS' medium, 12 mM $MgSO_4(7xH_2O)$) supplemented with DNAse. Cells were dissociated by triturating and adding HANKS' medium plus 20% FCS stopped the dissociation reaction. Cells were sedimented and seeded in PNGM^{TM}-medium (Lonza, CC-4462) on poly-L-lysine (Sigma, P9155)-coated glass coverslips at a density of 40,000 cells/cm^2. At 3 days in vitro (DIV) cells were transfected using Lipofectamine LTX (Invitrogen, 15,338,100). Live cell imaging, fixation, staining and analysis followed at indicated DIV.

Immunocytochemistry, colocalization analysis, and live-cell imaging

For immunocytochemistry, cells were cultured on cover slips, washed in PBS (137 mM NaCl, 2.7 mM KCl, 8.1 mM Na_2HPO_2, 1.47 mM KH_2PO_4), fixed in PBS with 4% paraformaldehyde and 4% sucrose (or with 100% ice-cold methanol for LC3 staining), washed and permeabilized with PBS with 0.5% saponin (Sigma, S7900) or 0.05% Triton X-100 (Roth, 3051.2). Cells were incubated with antibodies in the presence of 10% serum (Gibco, 10,270–160) and 0.5% saponin and analyzed by confocal microscopy using a Leica TCS SP8 microscope. For colocalization analysis, laser power and gain were identical between images. Using the Fiji ImageJ plugin JaCoP (ImageJ software; US National Institutes of Health, Bethesda) the Mander's coefficients for colocalization M1 and M2 were calculated. Bar graphs were produced using Graph Pad Prism 5 and statistically analyzed by a one-way analysis of variance (ANOVA) with a post hoc Tukey test (IBM SPSS Statistics 25).

For time-lapse video microscopy, cells were transfected with constructs encoding fluorophore tagged CLN3 and PSENEN fusion proteins in glass bottom dishes. During live-cell imaging, transfected cells were temperature- (37°C) and CO_2-controlled (5%). Images were taken every 200–300 ms over indicated periods using a spinning disk confocal microscope (Visitron Systems). Kymographs were created using the Multiple-Kymograph plugin of Fiji ImageJ.

For autophagic flux analysis, cells were seeded in glass bottom dishes and transfected with the tandem mCherry-GFP-LC3 construct. After 24–48 h, live imaging analysis was performed under control conditions or 6 h after starvation and the mCherry and GFP signals were recorded in parallel with a Leica TCS SP8 confocal microscope. The number of cellular vesicles per channel was counted by transforming the recorded confocal z-stacks into binary images applying an equal threshold between images and subsequently using the Fiji ImageJ function "analyze particles". Spatially close vesicles were separated using the Fiji ImageJ function "watershed" and background signals were ruled out by excluding single pixel counts. Bar graphs were produced using Graph Pad Prism 5. After confirming normal distribution using a Kolmogorov-Smirnov test, statistical differences were confirmed by one-way ANOVA with a post hoc Tukey test in IBM SPSS Statistics 25.

Immunoprecipitation

HeLa cells were transfected with constructs encoding HA-CLN3 and GFP-PSENEN or with HA-CLN3 and GFP. Twenty-four h post transfection, cells were lysed in 100 mM NaCl, 50 mM Tris-HCl, 1 mM $CaCl_2$, 1 mM $MgCl_2$, 0.5% NP40 (Sigma, 21–3277), 1 mM PMSF (Roth, 6367.1), pH 7.5, cell debris sedimented for 10 min at 16,000 g and 10% of each supernatant were taken as an expression control (input) and immunoprecipitation was performed using anti-GFP nanobody coupled to magnetic beads (ChromoTek, gtma-20) for 30 min at 4°C. After washing with 100 mM NaCl, 50 mM Tris-HCl, 1 mM $CaCl_2$, 1 mM $MgCl_2$, 0.01% Triton X-100, 1 mM PMSF, pH 7.5 protein complexes were subjected to SDS-PAGE and immunoblotting.

Immunoblotting

Protein concentration was determined using the bicinchoninic acid (BCA) method (BCA Protein Assay; Pierce, 23,227). Equal amounts of protein samples were mixed with SDS sample buffer, boiled at 95°C for 5 min, subjected to reducing SDS-PAGE using 4–16% acrylamide gels and transferred to PVDF membranes. Subsequently the membranes were incubated with primary antibodies, HRP-conjugated secondary antibodies, and ECL-solution (SuperSignalWest Pico; Thermo-scientific, 34,580). Chemiluminescence signals were detected with a LAS4000Mini system (Fuji). For quantification and statistical analysis, 6–10 independent experiments were performed. Bands of immunoblots were quantified by using Multi Gauge V3.2 (Fuji), Fiji ImageJ and a one-way ANOVA with a post hoc Dunnett's test for statistical analysis.

In situ hybridization

In situ hybridization was performed as described before [77]. In brief, antisense RNA probes labeled with α-^{35}S-UTP were generated according to the manufacturer's instructions (Ambion, 1344). Cryosections (20 μm) from C57BL/6 J mice (embryonic day 16) were fixed, acetylated, dehydrated, and subjected to in situ hybridization at 55°C for 18 h, followed by

RNaseA (AppliChem, A3832) treatment for 30 min at 37°C, and a high-stringency wash was performed in 0.1 x saline sodium citrate buffer (15 mM NaCl, 1.5 mM sodium citrate, pH 7) at 55°C. Slides were exposed to X-ray films (Kodak Biomax MR, Amersham Biosciences, Z363030) for 72 h. The probe used for detection of *Cln3* transcripts comprised nucleotides 1–653 of the murine cDNA cloned in pBSK (Stratagene, 212,205), which was linearized with NotI for antisense transcription. A cDNA clone (IMAGp998J21802Q, Source Bioscience) comprising the entire open reading frame and 5′- and 3′-UTR sequence of murine *Psenen* served as a template to clone the probe used for detection of *Psenen* transcripts into pBSK and comprised 594 nucleotides. This was linearized with NotI for the antisense probe. Specificity of signals was verified by comparing antisense with sense controls.

Generation of knockout cells

In order to generate knockout cells, guide RNA (gRNA) corresponding to the first exon of *CLN3* (CACCGCGGCGCTTTTCGGATTCCGA) and to the first exon of *PSENEN* (CACCGCCTGGAGCGAGTGTCCAATG) was designed and cloned into pX330-U6 expressing a humanized Cas9 [78]. HeLa cells were co-transfected with pX330-U6-gRNA-CLN3 or pX330-U6-gRNA-*PSENEN* and pcDNA3.1/Zeo. Twenty-four h after transfection, cells were selected with zeocin (250 μg/ml) for 5 days to enrich transfected cells. Subsequently, cells were cultured for 2 weeks in DMEM with 10% FCS, single clones were isolated, genomic DNA extracted and genomic sequences surrounding *CLN3* and *PSENEN* genes amplified by PCR and sequenced. DNA sequencing identified different knockout cell clones carrying specific indel mutations. Two differently targeted and independent *CLN3* KO clones and two independent *PSENEN* KO clones with identical mutations (Figure S2) were expanded and analyzed in parallel to exclude clonal effects. Results showed similar phenotypes. KO cells were continuously genotyped by PCR using respective genomic DNA extracted from cells, the primer pairs (5′-TTGTTCTAATAGGGGCGTGG and 5′-CCTCCTCTGTGCTCTAGACT) for *PSENEN* KO cells and (5′-CCAGCCCCTCCCTTTTTCACG and 5′-TGGGGCAAACCAGTGGATTCAG) for *CLN3* KO cells and sequencing of gel-extracted PCR products.

Cell growth analysis

Cells were seeded in 24-well plates at a density of 5,000 cells per well. Images were captured at identical areas in a 4 h interval for 8 days and confluence was measured using the IncuCyte S3 live cell imaging system (Sartorius). Data of each image was normalized individually and averaged over 4 wells. To compensate for variations within individually measured time points by the confluence mask, a rolling average using a window of 6 time points was applied. The time point of maximal growth (maximum slope) was used to set an interval

of 12 h before and 12 h after this time point for statistical analysis using two-sided Mann-Whitney U-tests.

Quantification of Aβ levels

Cell culture media (DMEM without FCS) was collected following conditioning for 24 h and cell debris removed by centrifugation. Secreted Aβ40 and Aβ42 peptides and sAPP-α were quantified by sandwich enzyme-linked immunosorbent assay according to the manufacturer's instructions (IBL, ELISA JP27729 human amyloid β and JP27734 human sAPP-α). All measurements were performed in triplicates. sAPP-α levels were almost identical between the cell lines. Aβ levels were normalized to sAPP-α levels. Statistical analysis was performed with GraphPad Prism using a one-way ANOVA with a post hoc Tukey test.

Lysosomal protease activity measurement

For the measurement of HEXA/β-hexosaminidase A activity, cells were lysed in 20 mM Tris-HCl, 150 mM NaCl, 10 mM EDTA, 1% Triton X-100, pH 8. Protein concentration was measured using the BCA method. From each cell lysate, 100 μg total protein was incubated with HEXA substrate (10 mM 4-nitrophenyl-N-acetyl-β-D-glucosaminide [Sigma, N9376], 100 mM sodium citrate, 0.2% Triton X-100, pH 4.6) for 30 min at 37°C. The reaction was stopped with 0.05 M glycine-NaOH, pH 10.4 and enzymatic activity determined as released 4-nitrophenol by measuring absorbance at 405 nm using a spectrophotometer (Amersham Biosciences). Statistical analysis was performed with GraphPad Prism using a one-way ANOVA with a post hoc Bonferroni test.

Lysosomal protease activity in cells was determined using DQ-red-BSA (Thermo Fisher Scientific, D12051) and CTSB activity was determined using Magic Red Cathepsin B (ImmunoChemistry Technologies, ICT-937). Cells were seeded at a density of 15,000 cells per well in poly-L-lysine coated 96-well plates. After 24 h, cells were incubated with 10 μg/μl DQ-red-BSA in DMEM with 1% FCS, 1% non-essential amino acids, 1% Glutamax (Invitrogen, 35,050–38), 1% HEPES for 1 h or 6 h. In parallel experiments, 100 nM bafilomycin A$_1$ (Biomol, cay11038-500) was added. To determine CTSB activity, cells were incubated with Magic Red staining solution diluted in DMEM with 1% FCS, 1% non-essential amino acids, 1% Glutamax, 1% HEPES to a 1-fold concentration at 37°C for 30 min, 180 min and 300 min respectively. After incubation, cells were washed once with PBS, stained with Hoechst (Thermo Fisher Scientific, H3570) for 5 min at 37°C and washed again three times with PBS. Fluorescence was measured using automated confocal microscopy (OPERA Phenix high content system, PerkinElmer) with a 20-fold magnification. Image analysis was performed with the Columbus and Spotfire software (PerkinElmer). Only living cells, distinguishable from dead cells via Hoechst staining, were used for analysis. Background from untreated wells was subtracted and fluorescence intensity was normalized to

the cell number. Statistical analysis was performed with GraphPad Prism using a two-way ANOVA and multiple comparison with a post hoc Tukey test which is using a single pooled variance for calculations.

TF uptake assay

Twenty-four h after transfection with GFP, cells were starved 1 h at 37°C in Opti-MEM (Gibco, 11,058,021) and labeled 1 h at 4°C with 50 µg/ml fluorescent transferrin-Alexa Fluor 555 (Thermo Fisher Scientific, T35352) in Opti-MEM. After washing, cells were incubated for different time intervals at 37°C. Cells were fixed with 4% paraformaldehyde and stained with primary anti-GFP and secondary Alexa Fluor 488 antibodies. The GFP signal (Alexa Fluor 488) was used to visualize cells. Fluorescent vesicles (Alexa Fluor 555) per cell were determined by confocal microscopy using identical laser power and gain between images and the "analyze particles" function of the Fiji ImageJ software. Bar graphs were produced using Graph Pad Prism 5. After confirming normal distribution using a Kolmogorov-Smirnov test, statistical differences were confirmed by one-way ANOVA with a post hoc Tukey test in IBM SPSS Statistics 25.

Gene expression analysis by quantitative real-time PCR

Cells were treated as indicated and total RNA extracted using Trizol (Thermo Fisher Scientific, 15,596,026). RNA integrity was assessed by inspection of *RNA18S* and *RNA28S* ribosomal RNA bands using agarose gel-electrophoresis and quantity was determined by optical density measurement using NanoDrop 2000 (Thermo Scientific).

We performed expression analysis as described before [79]. In brief, residual genomic DNA was removed and one µg total RNA per reaction was reverse transcribed to cDNA by using oligo dT primers as well as hexamer primers and SuperScript IV according to the manufacturer's instructions (VILO Mastermix with ezDNase, Thermo Fisher Scientific, 11,766,050). Gene expression levels were determined by quantitative real-time PCR performed in a QuantStudio 6 Flex Real-Time PCR System (Applied Biosystems). We used the following Fam labeled TaqMan Gene Expression Assays (Thermo Fisher Scientific) to detect expression of genes of interest: *CLN3*: Hs00164002_m1; *CTSB*: Hs00157194_m1; *CTSD*: Hs00157201_m1; *GLB1*: Hs01035168_m1; *PSENEN*: Hs01033961_g1; *PSAP*: Hs01551096_m1; *PSEN2*: Hs00240982_m1; *SESN2*: Hs00230241_m1; *TFEB*: Hs00292981_m1 and *TPP1*: Hs00166099_m1. All assays were exon-spanning with similar amplicon length. Prior to the determination of the relative differences in expression levels of the genes of interest, the three different Vic labeled TaqMan Gene Expression Assays *APRT*: Hs00356991_m1; *HPRT*: Hs02800695_m1 and *TBP*: Hs00427620_m1 were evaluated for their suitability as reference genes by analyzing their expression stability under the different conditions analyzed in this study. To this end, we used the RefFinder software, which combines the results of four different software packages for the stability of expression analysis [80]. Best performance was observed for *APRT* and *HPRT* and we chose *APRT* as reference for duplex assays, because its expression level was similar to that of our genes of interest. In control experiments, the complete RT-qPCR analysis of all cell lines was also performed with *HPRT* as a reference gene with a congruent outcome. We established duplex assays for the comparative analysis of expression of the genes of interest by determining the respective concentration of the transcript of interest and of the reference transcript by simultaneous detection in the same reaction. RT-qPCR was performed using TaqMan Gene Expression master mix (Thermo Fisher Scientific, 4,369,542) in a 384-well format, reaction volumes were 10 µl and the number of replicates per sample was three. We applied the following thermal cycling conditions: activation of hot-start Taq DNA Polymerase at 95°C for 10 min and two-step cycling with denaturation at 95°C for 15 s, annealing and extension at 60°C for 60 s and fluorescence data collection run in 40 cycles. Differential gene expression was calculated with the Relative Quantification app (Version 3.8, Thermo Fisher), using the individually determined efficiencies of the respective targets for the ΔΔ-Ct determinations. The REST software was utilized to evaluate the significance of the relative differences [81].

Statistical analysis

Statistical tests were performed using Graph-Pad Prism or IBM SPSS Statistics software and analyzed by a one-way analysis of variance (ANOVA) with a post hoc Tukey test or a post hoc Bonferroni test or two-way ANOVA and multiple comparison with a post hoc Tukey test. For gene expression analysis, the REST software was utilized to evaluate the significance of the relative differences.

Ethics approval

No experiments on living animals were conducted for this study. Housing and scarification of animals as well as use of animal material in this study were ethically reviewed and carried out in accordance with European Directive 2010/63/EEC and local policies on the care, welfare and treatment of animals.

ORCID

Guido Hermey http://orcid.org/0000-0003-4762-5262

References

[1] Takasugi N, Tomita T, Hayashi I, et al. The role of presenilin cofactors in the gamma-secretase complex. Nature. 2003 Mar 27;422(6930):438–441.

[2] Kaether C, Haass C, Steiner H. Assembly, trafficking and function of gamma-secretase. Neurodegener Dis. 2006;3(4–5):275–283.

[3] Cai T, Tomita T. Structure-activity relationship of presenilin in γ-secretase-mediated intramembrane cleavage. Semin Cell Dev Biol. 2020 Mar;105:102–109.

[4] De Strooper B. Aph-1, Pen-2, and Nicastrin with Presenilin generate an active gamma-Secretase complex. Neuron. 2003 Apr 10;38(1):9–12.

[5] Lichtenthaler SF, Haass C, Steiner H. Regulated intramembrane proteolysis–lessons from amyloid precursor protein processing. J Neurochem. 2011 Jun;117(5):779–796.

[6] Eggert S, Thomas C, Kins S, et al. Trafficking in alzheimer's disease: modulation of app transport and processing by the transmembrane proteins LRP1, SorLA, SorCS1c, Sortilin, and calsyntenin. Mol Neurobiol. 2018 Jul;55(7):5809–5829.

[7] Wolfe MS. Unraveling the complexity of γ-secretase. Semin Cell Dev Biol. 2020 Jan;105:3–11.

[8] Wang B, Yang W, Wen W, et al. Gamma-secretase gene mutations in familial acne inversa. Science. 2010 Nov 19;330 (6007):1065.

[9] Hori K, Sen A, Artavanis-Tsakonas S. Notch signaling at a glance. J Cell Sci. 2013 May;126(Pt 10):2135–2140.

[10] Güner G, Lichtenthaler SF. The substrate repertoire of γ-secretase /presenilin. Semin Cell Dev Biol. 2020 Jun;105:27–42.

[11] Neely KM, Green KN, LaFerla FM. Presenilin is necessary for efficient proteolysis through the autophagy-lysosome system in a gamma-secretase-independent manner. J Neurosci. 2011 Feb 23;31(8):2781–2791.

[12] Nixon RA, Yang DS. Autophagy failure in Alzheimer's disease–locating the primary defect. Neurobiol Dis. 2011 Jul;43(1):38–45.

[13] Wilson CA, Murphy DD, Giasson BI, et al. Degradative organelles containing mislocalized alpha-and beta-synuclein proliferate in presenilin-1 null neurons. J Cell Biol. 2004 May;165(3):335–346.

[14] Esselens C, Oorschot V, Baert V, et al. Presenilin 1 mediates the turnover of telencephalin in hippocampal neurons via an autophagic degradative pathway. J Cell Biol. 2004 Sep;166 (7):1041–1054.

[15] Coen K, Flannagan RS, Baron S, et al. Lysosomal calcium homeostasis defects, not proton pump defects, cause endo-lysosomal dysfunction in PSEN-deficient cells. J Cell Biol. 2012 Jul 9;198 (1):23–35.

[16] Lee JH, McBrayer MK, Wolfe DM, et al. Presenilin 1 maintains lysosomal Ca(2+) homeostasis via TRPML1 by Regulating vATPase-mediated lysosome acidification. Cell Rep. 2015 Sep 1;12(9):1430–1444.

[17] Lee JH, Yu WH, Kumar A, et al. Lysosomal proteolysis and autophagy require presenilin 1 and are disrupted by Alzheimer-related PS1 mutations. Cell. 2010 Jun 25;141 (7):1146–1158.

[18] Whyte LS, Lau AA, Hemsley KM, et al. Endo-lysosomal and autophagic dysfunction: a driving factor in Alzheimer's disease? J Neurochem. 2017 Mar;140(5):703–717.

[19] Zhang X, Garbett K, Veeraraghavalu K, et al. A role for presenilins in autophagy revisited: normal acidification of lysosomes in cells lacking PSEN1 and PSEN2. J Neurosci. 2012 Jun 20;32 (25):8633–8648.

[20] Meckler X, Checler F. Presenilin 1 and presenilin 2 target gamma-secretase complexes to distinct cellular compartments. J Biol Chem. 2016 Jun 10;291(24):12821–12837.

[21] Sannerud R, Esselens C, Ejsmont P, et al. Restricted location of PSEN2/gamma-secretase determines substrate specificity and generates an intracellular abeta pool. Cell. 2016 Jun 30;166 (1):193–208.

[22] Nugent T, Mole SE, Jones DT. The transmembrane topology of batten disease protein CLN3 determined by consensus computational prediction constrained by experimental data. FEBS Lett. 2008 Apr 2; 582(7):12821–12837.

[23] Cotman SL, Starpoli JF. The juvenile batten disease protein, CLN3, and its role in regulating anterograde and retrograde post-Golgi trafficking. Clin Lipidol. 2012;7(1):79–91.

[24] Lerner TJ, Boustany R-MN, Anderson JW, International-Batten-Disease-Consortium. Isolation of a novel gene underlying batten disease, CLN3. Cell. 1995;82(6):949–957.

[25] Kollmann K, Uusi-Rauva K, Scifo E, et al. Cell biology and function of neuronal ceroid lipofuscinosis-related proteins. Biochim Biophys Acta. 2013 Nov;1832(11):1866–1881.

[26] Butz ES, Chandrachud U, Mole SE, et al. Moving towards a new era of genomics in the neuronal ceroid lipofuscinoses. Biochim Biophys Acta Mol Basis Dis. 2020 Sep;1866(9):165571.

[27] Anderson GW, Goebel HH, Simonati A. Human pathology in NCL. Biochim Biophys Acta. 2013 Nov;1832(11):1807–1826.

[28] Herva R, Tyynela J, Hirvasniemi A, et al. Northern epilepsy: a novel form of neuronal ceroid-lipofuscinosis. Brain Pathol. 2000 Apr;10(2):215–222.

[29] Wisniewski KE, Kida E, Gordon-Majszak W, et al. Altered amyloid beta-protein precursor processing in brains of patients with neuronal ceroid lipofuscinosis. Neurosci Lett. 1990 Nov 27;120 (1):94–96.

[30] Wisniewski KE, Maslinska D, Kitaguchi T, et al. Topographic heterogeneity of amyloid B-protein epitopes in brains with various forms of neuronal ceroid lipofuscinoses suggesting defective processing of amyloid precursor protein. Acta Neuropathol. 1990;80(1):26–34.

[31] Cheng R, Tang M, Martinez I, et al. Linkage analysis of multiplex caribbean hispanic families loaded for unexplained early-onset cases identifies novel Alzheimer's disease loci. Alzheimers Dement (Amst). 2018;10:554–562.

[32] Qureshi YH, Patel VM, Berman DE, et al. An Alzheimer's disease-linked loss-of-function cln5 variant impairs cathepsin d maturation, consistent with a retromer trafficking defect. Mol Cell Biol. 2018 10;38(20). 10.1128/MCB.00011-18

[33] Kousi M, Lehesjoki AE, Mole SE. Update of the mutation spectrum and clinical correlations of over 360 mutations in eight genes that underlie the neuronal ceroid lipofuscinoses. Hum Mutat. 2012 Jan;33(1):42–63.

[34] Oetjen S, Kuhl D, Hermey G. Revisiting the neuronal localization and trafficking of CLN3 in juvenile neuronal ceroid lipofuscinosis. J Neurochem. 2016 Nov;139(3):456–470.

[35] Storch S, Pohl S, Braulke T. A dileucine motif and a cluster of acidic amino acids in the second cytoplasmic domain of the batten disease-related CLN3 protein are required for efficient lysosomal targeting. J Biol Chem. 2004 Dec 17;279 (51):53625–53634.

[36] Kyttala A, Ihrke G, Vesa J, et al. Two motifs target Batten disease protein CLN3 to lysosomes in transfected nonneuronal and neuronal cells. Mol Biol Cell. 2004 Mar;15(3):1313–1323.

[37] Kyttala A, Yliannala K, Schu P, et al. AP-1 and AP-3 facilitate lysosomal targeting of Batten disease protein CLN3 via its dileucine motif. J Biol Chem. 2005 Mar 18;280(11):10277–10283.

[38] Mao Q, Xia H, Davidson BL. Intracellular trafficking of CLN3, the protein underlying the childhood neurodegenerative disease, Batten disease. FEBS Lett. 2003 Dec 4;555(2):351–357.

[39] Schroder B, Wrocklage C, Pan C, et al. Integral and associated lysosomal membrane proteins. Traffic. 2007 Dec;8(12):1676–1686.

[40] Cao Y, Espinola JA, Fossale E, et al. Autophagy is disrupted in a knock-in mouse model of juvenile neuronal ceroid lipofuscinosis. J Biol Chem. 2006 Jul 21;281(29):20483–20493.

[41] Schmidtke C, Tiede S, Thelen M, et al. Lysosomal proteome analysis reveals that CLN3-defective cells have multiple enzyme deficiencies associated with changes in intracellular trafficking. J Biol Chem. 2019 06; 294(24): 9592–9604.

[42] Fossale E, Wolf P, Espinola JA, et al. Membrane trafficking and mitochondrial abnormalities precede subunit c deposition in a cerebellar cell model of juvenile neuronal ceroid lipofuscinosis. BMC Neurosci. 2004 Dec 10;5:57.

[43] Lojewski X, Staropoli JF, Biswas-Legrand S, et al. Human iPSC models of neuronal ceroid lipofuscinosis capture distinct effects of TPP1 and CLN3 mutations on the endocytic pathway. Hum Mol Genet. 2014 Apr;23(8):2005–2022.

[44] Yasa S, Modica G, Sauvageau E, et al. CLN3 regulates endosomal function by modulating Rab7A-effector interactions. J Cell Sci. 2020 Mar;133(6). 10.1242/jcs.234047.

[45] Ramirez-Montealegre D, Pearce DA. Defective lysosomal arginine transport in juvenile Batten disease. Hum Mol Genet. 2005 Dec;14 (23):3759–3773.

[46] Metcalf DJ, Calvi AA, Seaman M, et al. Loss of the Batten disease gene CLN3 prevents exit from the TGN of the mannose 6-phosphate receptor. Traffic. 2008 Nov;9(11):1905–1914.

[47] Brajenovic M, Joberty G, Kuster B, et al. Comprehensive proteomic analysis of human Par protein complexes reveals an interconnected protein network. J Biol Chem. 2004 Mar 26;279 (13):12804–12811.

[48] Holmes O, Paturi S, Selkoe DJ, et al. Pen-2 is essential for gamma-secretase complex stability and trafficking but partially dispensable for endoproteolysis. Biochemistry. 2014 Jul 15;53 (27):4393–4406.

[49] Prokop S, Shirotani K, Edbauer D, et al. Requirement of PEN-2 for stabilization of the presenilin N-/C-terminal fragment heterodimer within the gamma-secretase complex. J Biol Chem. 2004 May 28 279(22):23255–23261.

[50] Bammens L, Chávez-Gutiérrez L, Tolia A, et al. Functional and topological analysis of Pen-2, the fourth subunit of the gamma-secretase complex. J Biol Chem. 2011 Apr;286(14):779–796.

[51] Kopan R, Schroeter EH, Weintraub H, et al. Signal transduction by activated mNotch: importance of proteolytic processing and its regulation by the extracellular domain. Proc Natl Acad Sci U S A. 1996 Feb 20;93(4):1683–1688.

[52] Kucera A, Bakke O, Progida C. The multiple roles of Rab9 in the endolysosomal system. Commun Integr Biol. 2016 Jul-Aug;9(4): e1204498.

[53] Klionsky DJ, Abdel-Aziz AK, Abdelfatah S, et al. Guidelines for the use and interpretation of assays for monitoring autophagy. Autophagy. 2021Jan; 171: 1–382(4th edition)(1)

[54] Bajaj L, Lotfi P, Pal R, et al. Lysosome biogenesis in health and disease. J Neurochem. 2018 Aug 9;148:573–589.

[55] Sardiello M, Palmieri M, Di Ronza A, et al. A gene network regulating lysosomal biogenesis and function. Science. 2009 Jul 24;325(5939):473–477.

[56] Chan CH, Mitchison HM, Pearce DA. Transcript and in silico analysis of CLN3 in juvenile neuronal ceroid lipofuscinosis and associated mouse models. Hum Mol Genet. 2008 Nov 1;17(21):3332–3339.

[57] Kitzmuller C, Haines RL, Codlin S, et al. A function retained by the common mutant CLN3 protein is responsible for the late onset of juvenile neuronal ceroid lipofuscinosis. Hum Mol Genet. 2008 Jan 15;17(2):303–312.

[58] Jarvela I, Lehtovirta, M, Tikkanen, R, et al. Defective intracellular transport of CLN3 is the molecular basis of Batten disease (JNCL). Hum Mol Genet. 1999 Jun;8(6):1091–1098.

[59] Zhong Y, Mohan K, Liu J, et al. Loss of CLN3, the gene mutated in juvenile neuronal ceroid lipofuscinosis, leads to metabolic impairment and autophagy induction in retinal pigment epithelium. Biochim Biophys Acta Mol Basis Dis. 2020 Oct 1;1866(10):165883.

[60] Katz ML, Shibuya H, Liu PC, et al. A mouse gene knockout model for juvenile ceroid-lipofuscinosis (Batten disease). J Neurosci Res. 1999 Aug 15;57(4):551–556.

[61] Mitchison HM, Bernard DJ, Greene ND, et al. Targeted disruption of the Cln3 gene provides a mouse model for batten disease. the batten mouse model consortium [corrected]. Neurobiol Dis. 1999 Oct;6(5):321–334.

[62] Cotman SL, Vrbanac, V, Lebel, LA, et al. Cln3(Deltaex7/8) knock-in mice with the common JNCL mutation exhibit progressive neurologic disease that begins before birth. Hum Mol Genet. 2002 Oct 15;11(22):2709–2721.

[63] Cao Y, Staropoli JF, Biswas S, et al. Distinct early molecular responses to mutations causing vLINCL and JNCL presage ATP synthase subunit C accumulation in cerebellar cells. PLoS One. 2011 Feb 17;6(2):e17118.

[64] Chandrachud U, Walker MW, Simas AM, et al. Unbiased cell-based screening in a neuronal cell model of batten disease highlights an interaction between Ca2+ homeostasis, autophagy, and CLN3 protein function. J Biol Chem. 2015 Jun 5;290 (23):2709–2721.

[65] Medina DL, Fraldi A, Bouche V, et al. Transcriptional activation of lysosomal exocytosis promotes cellular clearance. Dev Cell. 2011 Sep 13;21(3):421–430.

[66] Palmieri M, Pal R, Nelvagal HR, et al. mTORC1-independent TFEB activation via Akt inhibition promotes cellular clearance in neurodegenerative storage diseases. Nat Commun. 2017 Feb 6;8:14338.

[67] Xiao Q, Yan P, Ma X, et al. Neuronal-Targeted TFEB accelerates lysosomal degradation of app, reducing abeta generation and amyloid plaque pathogenesis. J Neurosci. 2015 Sep 2;35 (35):12137–12151.

[68] Zhang QC, Petrey D, Deng L, et al. Structure-based prediction of protein-protein interactions on a genome-wide scale. Nature. 2012 Oct 25;490(7421):556–560.

[69] Kotlyar M, Pastrello C, Malik Z, et al. IID 2018 update: context-specific physical protein-protein interactions in human, model organisms and domesticated species. Nucleic Acids Res. 2019 Jan 8;47(D1):D581–D589.

[70] Reddy K, Cusack CL, Nnah IC, et al. Dysregulation of nutrient sensing and clearance in presenilin deficiency. Cell Rep. 2016 Mar 8;14(9):2166–2179.

[71] Hermey G, Schmidt N, Bluhm B, et al. SorCS1 variants and amyloid precursor protein (APP) are co-transported in neurons but only SorCS1c modulates anterograde APP transport. J Neurochem. 2015 Oct;135(1):60–75.

[72] N'Diaye EN, Kajihara KK, Hsieh I, et al. PLIC proteins or ubiquilins regulate autophagy-dependent cell survival during nutrient starvation. EMBO Rep. 2009 Feb;10(2):173–179.

[73] Van Engelenburg SB, Palmer AE. Imaging type-III secretion reveals dynamics and spatial segregation of Salmonella effectors. Nat Methods. 2010 Apr;7(4):325–330.

[74] Shevchenko A, Wilm M, Vorm O, et al. Mass spectrometric sequencing of proteins silver-stained polyacrylamide gels. Anal Chem. 1996 Mar 1;68(5):850–858.

[75] Nielsen MS, Keat SJ, Hamati JW, et al. Different motifs regulate trafficking of SorCS1 isoforms. Traffic. 2008 Jun;9(6):980–994.

[76] Oetjen S, Mahlke C, Hermans-Borgmeyer I, et al. Spatiotemporal expression analysis of the growth factor receptor SorCS3. J Comp Neurol. 2014 Oct 15;522(15):3386–3402.

[77] Denkena J, Zaisser A, Merz B, et al. Neuronal activity regulates alternative exon usage. Mol Brain. 2020 Nov 10;13(1):148.

[78] Cong L, Ran FA, Cox D, et al. Multiplex genome engineering using CRISPR/Cas systems. Science. 2013 Feb 15;339 (6121):819–823.

[79] Hermey G, Hoffmeister-Ullerich SA, Merz B, et al. Amyloidosis causes downregulation of SorLA, SorCS1 and SorCS3 expression in mice. Biol Chem. 2019 Aug 27;400(9):1181–1189.

[80] Xie F, Xiao P, Chen D, et al. miRDeepFinder: a miRNA analysis tool for deep sequencing of plant small RNAs. Plant Mol Biol. 2012 Jan;80 (1):75–84.

[81] Pfaffl MW. Relative expression software tool (REST) for group-wise comparison and statistical analysis of relative expression results in real-time PCR. Nucleic Acids Res. 2002 May;30(9):e36.